# River and Hillslope Response to Localized Uplift Along a Left Bend of the San Andreas Fault, Santa Cruz Mountains, CA

S. Connor Kee

A report prepared in partial fulfillment of
the requirements for the degree of

Master of Science
Earth and Space Sciences: Applied Geosciences

University of Washington

June, 2016

Project Mentor:
Alison Duvall

Internship Coordinator:
Kathy Troost

Reading committee:
Alison Duvall
Steven Walters

MESSAGe Technical Report Number: 036

## Executive Summary

Studying landscape evolution of the Earth's surface is difficult because both tectonic forces and surface processes control its response to perturbation, and ultimately, its shape and form. Researchers often use numerical models to study erosional response to deformation because there are rarely natural settings in which we can evaluate both tectonic activity and topographic response over appropriate time scales ($10^3$-$10^5$ years). In certain locations, however, geologic conditions afford the unique opportunity to study the relationship between tectonics and topography. One such location is along the Dragon's Back Pressure Ridge in California, where the landscape moves over a structural discontinuity along the San Andreas Fault and landscape response to both the initiation and cessation of uplift can be observed. In their landmark study, Hilley and Arrowsmith (2008) found that geomorphic metrics such as channel steepness tracked uplift and that hillslope response lagged behind that of rivers. Ideal conditions such as uniform vegetation density and similar lithology allowed them to view each basin as a developmental stage of response to uplift only. Although this work represents a significant step forward in understanding landscape response to deformation, it remains unclear how these results translate to more geologically complex settings.

In this study, I apply similar methodology to a left bend along the San Andreas Fault in the Santa Cruz Mountains, California. At this location, the landscape is translated through a zone of localized uplift caused by the bend, but vegetation, lithology, and structure vary. I examine the geomorphic response to uplift along the San Andreas Fault bend in order to determine whether predicted landscape patterns can be observed in a larger, more geologically complex setting than

the Dragon's Back Pressure Ridge. I find that even with a larger-scale and a more complex setting, geomorphic metrics such as channel steepness index remain useful tools for evaluating landscape evolution through time. Steepness indices in selected streams of study record localized uplift caused by the restraining bend, while hillslope adjustment in the form of landsliding occurs over longer time scales. This project illustrates that it is possible to apply concepts of landscape evolution models to complex settings and is an important contribution to the body of geomorphological study.

## Table of Contents

## List of Figures

## List of Tables

## Acknowledgements

I would like to thank my mentor and Master's Supervisory Committee chair, Alison Duvall, for suggesting this project and for her continued support and enthusiasm. I thank Steven Walters and Kathy Troost, for their guidance and support in this process, and for serving on my MSC. I am also grateful to my colleagues Dottie Metcalf-Lindenburger and Patrick Kao for their insightful revisions, and to Sarah Harbert for her timely advice regarding Stream Profiler and steepness calculations.

## Introduction & Project Motivation

Tectonic geomorphologists regularly glean valuable information regarding underlying structures, tectonic driving forces, and geodynamics by observing the evolution of landscapes through time (Burbank and Anderson, 2001). However, studying landscape evolution of the Earth's surface remains challenging because tectonic forces, surface processes, and atmospheric conditions (which all operate over variable spatial and temporal scales) control its response to perturbation, and ultimately, its shape and form. Furthermore, surface processes may vary with changing climates (Tucker and Slingerland, 1997) and different lithologic properties (Heimsath et al., 1997). In spite of these complications, advancements have been made in understanding how bedrock channel steepness (e.g., Snyder et al., 2000; Whipple and Tucker, 1999), basin relief (e.g., Lague et al., 2003), and basin elevation (e.g., Willgoose et al., 1991) vary with uplift rates. Often these studies focus on a single surface process, such as bedrock channel incision (e.g., Whipple and Tucker, 1999); however, the interaction between hillslopes and rivers in response to uplift may be key in understanding the overall topographic adjustments to tectonic activity. Researchers often use numerical models to study erosional response to deformation because there are rarely natural settings in which we can evaluate both tectonic activity and topographic response over appropriate time scales ($10^3$-$10^5$ years) (e.g., Howard, 1994; van der Beek and Braun, 1998; Willgoose et al., 1991; Tucker, 2004). However, most recognize that field validation of these models is needed in order to fully understand the relationship between tectonics and topography (Tucker and Hancock, 2010).

The motivation for this project comes from one such field-based study by Hilley and Arrowsmith (2008), who examined geomorphic responses to uplift along the Dragon's Back Pressure Ridge (DBPR) in California. The landscape is moved along the San Andreas Fault (SAF), and passes through a zone of localized uplift (the "Dragon's Back") created by a change in dip at depth (a "structural knuckle") at the southeastern end of the ridge. Ideal conditions such as uniform vegetation density and similar lithology allowed Hilley and Arrowsmith (2008) to view each river basin as a developmental stage of response to uplift (a space-for-time-substitution). Therefore, this area provides a unique opportunity to study channel and hillslope response to localized uplift and to examine the relationship between tectonics and topography. The study utilized geologic mapping, aerial photography, and airborne laser swath mapping data to evaluate how erosional processes changed with the initiation and cessation of this uplift, as well as how geomorphic metrics such as channel steepness and longitudinal profile concavity reflected these changes. Although the DBPR provides an important field-based assessment of landscape evolution in response to uplift, it is unclear whether metrics such as channel steepness are robust enough to produce similar results in more complex settings.

In this study, I apply similar methodology to the landscape surrounding a restraining bend in the SAF in the Santa Cruz Mountains (SCM), California (Figure 1). At this location, a left bend in fault strike creates a zone of localized uplift. In this way, the SCM is similar to the DBPR even though the structural geometry that creates relief in each location is different. Also in contrast to the DBPR, climatic, lithologic, and structural conditions vary throughout the SCM and the uplifted are is much larger in scale than the DBPR. While the DBPR is ~4.5 km long with a maximum relief of 60 m, the SCM study area is 75 km long and exhibits a maximum relief of

~1150 m. Drainage basin areas are less than 0.5 $km^2$ in the DBPR, whereas they range from ~5 – ~80 $km^2$ in the SCM. I examine the geomorphic response to uplift along the SAF in order to determine whether broad patterns of landscape response can be observed in a larger, more geologically complex setting than the DBPR.

## Background

*Project Motivation: Results from the Dragon's Back Pressure Ridge*

Work by Hilley and Arrowsmith (2008) along the DBPR sets the groundwork for this study by showcasing field validation of landscape evolution models in a fortuitous geologic setting. In order to gain a complete understanding of topographic response to uplift, the next step is to apply this methodology to larger scale landscapes with a more complex geologic setting. Here, I discuss the findings of Hilley and Arrowsmith (2008) in detail because I use them for direct comparison with the results of this study.

A key element in the Hilley and Arrowsmith (2008) study was the space-for-time substitution used to produce a time series of deformation across the ridge. Using a slip rate between 32 and 35 mm/yr along this stretch of the SAF, they calculated that each kilometer along the ~4.5 km ridge represents ~33 k.y. While they primarily intended to use the space-for-time substitution to infer rock uplift rates, they also applied it to topographic changes; uniform vegetation density and similar lithology allowed them to view each basin as a developmental stage of response to

uplift. Thus, this made it possible to reconstruct a deformation history for a given basin and examine overall changes in channel and hillslope morphology at various points along the ridge.

Changes in residual relief, basin width, basin area, channel concavity, and normalized channel steepness were also analyzed along the DBPR (Figure 2). The results of Hilley and Arrowsmith (2008) indicated that channel steepness tracks rock uplift, while concavity and relief peak after uplift ceases. Additionally, basin width and area increased with distance northwest along the DBPR. In terms of hillslope response, hillslope gradient and landslide scar density peak in the wake of the uplift zone (Figure 2). Decreasing channel steepness and increasing concavity following uplift were accompanied by channel incision and undercutting of hillslopes, triggering landslides. The increase in concavity also correlated with increasing relief, caused by channel downcutting.

Channel downcutting continued for 0.2 km past the uplift zone, indicating that channels take ~6.6 k.y. to respond to uplift along the DBPR. A gradual transition from mass wasting to diffusive hillslope transport proceeded for ~2.2 km, signifying that hillslopes take ~73 k.y. to respond. Thus, they found that hillslopes along the DBPR take an order of magnitude longer to respond to uplift than channels. This difference in response time influences landform relief as well as distribution of erosive processes through time. Such a delayed hillslope response may be surprising in quickly adjusting settings (Whipple and Tucker, 1999); however, despite the fact that widespread landsliding (initiated by undercutting of hillslopes) allows for initially rapid hillslope response, the return to diffusive processes produces a lag in response time (e.g., Fernandes and Dietrich, 1997).

It is important to note that in this study I do not intend to prove or disprove the findings of Hilley and Arrowsmith (2008). Rather, I assume that their findings are representative of an accurate, field-based landscape evolution model in a relatively simple geologic setting and aim to determine whether complexities in the landscape interfere with these metrics.

*Geologic Setting & Previous Studies: Santa Cruz Mountains Field Site*

The SCM are located between the San Francisco Bay area and Monterey Bay in California. As with many ranges along the Pacific coast, the SCM are associated with an active fault system (the SAF and related faults) that closely follows the plate boundary between the North American and Pacific plates. Many smaller fault systems run parallel to the SAF; the Zayante-Vergeles and Butano faults are most relevant to this project because they cut through the streams of study (Figure 3). The Zayante-Vergeles fault (ZVF) is a dextral reverse-oblique-slip fault that runs for 87 km from north of Ben Lommond Mountain to south of Pajaro Valley. The most recent vertical movement in this zone occurred in the Pleistocene and possibly the Holocene at a slip rate of 0.2 mm/yr (Coppersmith, 1979); although vertical movement appears to have dominated late Cenozoic offset, Coppersmith (1979) argues that there are equal components of vertical and lateral movement. The Butano fault (BF), which extends for 46 km from San Gregorio to the SAF; it exhibits right lateral motion similar to the other faults discussed here at slip rate of less than 0.2 mm/yr (Quaternary Fault and Fold Database of the United States). Also of note is the San Gregorio fault zone (SGF), located mostly offshore, which does not cut through any of the

selected streams but possibly exerts influence on the uplift rates obtained from marine terraces along the coast (Gudmundsdottir et al., 2013; Figure 3).

The lithology of the study section of the SCM consists of Cretaceous crystalline basement rocks overlain by Tertiary sedimentary rocks, with Quaternary sediments filling in low-lying valleys (Graymer et al., 2006b; Figure 4). The crystalline basement includes igneous intrusive (gabbro, granite, and quartz diorite) and high-grade metasedimentary rocks (schist, quartzite, and marble); exposure of these units is largely limited to the Ben Lommond Mountain area, outside the range of the basins studied in this project (Clark and Rietman, 1973). The remainder of the study area is composed of Tertiary and Quaternary marine clastic sedimentary rocks (sandstones, siltstones, and mudstones) with a total thickness of 22,000 ft; these units can be divided into four continuous sequences, each bounded by unconformities (Clark and Rietman, 1973; Figure 5).

As noted in the introduction, topography and uplift of the SCM is closely associated with a left bend in the SAF (Figure 1), which imparts a localized uplift similar to that of the DBPR (Aydin and Page, 1984; Anderson 1990, 1994; Schwartz et al., 1990; Valensise and Ward, 1991; Aydin et al., 1992; Bürgmann et al., 1994). The northern SCM, located to the southwest of the SAF, are dominated by warping and folding likely caused by movement through the bend (Bürgmann et al., 1994). According to Anderson (1990) and Valensise and Ward (1991), recurring earthquakes such as the magnitude 7.1 1989 Loma Prieta earthquake cause uplift in this section of the SCM. In the southern SCM, located northeast of the SAF, a deep reverse fault system creates a well-defined zone of uplift (McLaughlin et al., 1988). Here, Loma Prieta remains the highest peak in

the SCM despite models indicating subsidence. Thus, an additional uplift mechanism is thought to account for the high topography where uplift rate exceeds denudation rate (Anderson, 1990).

Over the last 3 million years, uplift rates near the Loma Prieta epicenter southwest of the SAF have reached 0.5 mm/yr (Anderson, 1990) (Figure 6). The Pacific plate moves northwest relative to the North American plate along the bend at a rate of 10 - 20 mm/yr, and maximum uplift in the area (northern SCM, southwest of the SAF) is thought to be 1 - 3 km (Anderson, 1990). Marine terraces along the Santa Cruz coastline are important for evaluating uplift over several hundred thousand years. Ancient mean sea level, represented by the elevations of the inner edges of wave-cut platforms, and global sea level curves allow the assignment of terrace ages (Figure 6). The SCM provide an excellent opportunity to study landscape response to a fault bend and to a point source of localized uplift. Anderson (1990) noted the qualities that make this site interesting for study: 1) long-term uplift rates can be inferred, 2) faults and slip rates are well-known, 3) coseismic uplift patterns can be inferred from the 1989 Loma Prieta earthquake, and 4) erosion rates are available.

Several previous studies have examined erosion and uplift rates within the SCM. Bürgmann et al. (1994) found that the apatite fission track system northeast of the bend was reset in the late Cenozoic, but has not been reset southwest of the bend since the late Mesozoic. Bürgmann et al. (1994) subsequently estimated an exhumation rate of ~0.8 mm/yr in the Sierra Azul northeast of the SAF. Marine terraces stretch along the coast from Santa Cruz to Half Moon Bay and archive uplift from the last 100 – 500 k.y. (Bradley and Griggs, 1976; Lajoie et al., 1979; Anderson, 1990). Weber and Allwardt (2001) presented terrace age correlations in which maximum uplift

rates reached 0.6 – 0.7 mm/yr; when extrapolated inland from the coast, this maximum uplift rate corresponds to the area within the left bend. Cosmogenic $^{10}$Be depth profile dating of the terraces by Perg et al. (2001) suggests that the terraces may be half as old as previously thought, in which case the uplift rates would be 1.2 – 1.4 mm/yr in the bend. Distribution of uplift near the bend is consistent with surface deformation from the 1989 Loma Prieta earthquake (Valensise and Ward, 1991).

Recently, Gudmundsdottir et al. (2013) obtained $^{10}$Be-derived denudation rates from river sands in the SCM (Figure 7). These denudation rates were used as a proxy for uplift rates by assuming that the landscape is near steady-state (e.g., Willet and Brandon, 2002). Since steady state is approached by landscapes in which consistent uplift outlasts the time scale of geomorphic response ($10^4$ – $10^6$ years; Whipple and Tucker, 1999), Gudmundsdottir et al. (2013) note that the SCM have been uplifting for at least 5 m.y. and claim that they are therefore near steady-state. In contrast, they point out areas of high elevation but low relief, such as Ben Lommond Mountain to the southwest (Figure 1), are indicative of landscapes in disequilibrium (i.e., still adjusting to recent perturbation) (DiBiase et al., 2010), and are thus omitted from this study. It is important to note, however, that the presence of knickpoints in the SCM (discussed below) calls the assertions into question. Increases in denudation rates are well-correlated with the increasing uplift rates determined by apatite fission track and terrace dating; results from all three of these methods indicate between 0.6 – 0.8 mm/yr of uplift within the bend. As Gudmundsdottir et al. (2013) note, this consistency is significant considering the differences between the methods in terms of measured quantities and the range of timescales.

*Tectonics from Topography: Channel Profile Analysis*

Analysis of bedrock channel profiles is an integral part of tectonic geomorphology investigations because river incision controls the rate and style of landscape response to tectonic forcing and their form often conveys information about the rate and timing of base level fall (Whipple and Tucker, 1999; Kirby and Whipple, 2012). Hack (1957, 1973) noted that typical bedrock river profiles are described by a power-law relationship between slope (*S*) and upstream drainage area (*A*); this relationship was later formalized by Flint (1974) as:

$$S = k_s A^{-\theta} \quad (1)$$

where $k_s$ is the steepness index and $\theta$ is the concavity index (both unitless). Upstream basin shape determines the increase in downstream discharge, which in turn influences the rate of profile slope adjustment, i.e. the concavity of the profile (Hack, 1957; Figure 8). The relationship described by Equation (1) applies only past a critical drainage area that typically lies between 0.1 – 5km$^2$ (Montgomery and Foufoula-Georgiou, 1993). Within this range, there is a transition (either sudden or gradual) from debris flow dominated colluvial channels to fluvial channels (Stock and Dietrich, 2003; Figure 9). Changes in lithology, uplift rate, or climate may cause the fluvial section of the profile to contain multiple segments, each with their own steepness and concavity values (Wobus et al., 2006a). Study of variations in the concavity index among streams reveals that concavity typically falls within the narrow range of 0.4 – 0.6 (Snyder et al., 2000; Wobus et al., 2006a; Kirby and Whipple, 2012). However, studies also show that concavity is influenced by changes in lithology (Duvall et al., 2004), in alluvial cover (Sklar and Dietrich, 2004), in uplift rate (Kirby and Whipple, 2001), and in runoff (Roe et al., 2002) along

the channel. Additionally, the concavity index is set by rates of increasing discharge versus channel width (Whipple and Tucker, 1999).

As long as lithology, uplift rate, and climate are constant along the length of a channel, concavity index remains relatively independent of these factors; steepness index, on the other hand, varies with these factors and is thus a broadly used tool in tectonic geomorphology studies (Wobus et al., 2006a). Channel steepness is widely recognized as a geomorphic metric that tracks uplift in bedrock channels where uplift and erosion are balanced (Whipple and Tucker, 1999), and has been a prominent component in numerous studies of landscape response to tectonic forcing (e.g., Snyder et al., 2000; Duvall et al., 2004; Whipple, 2004; Wobus et al., 2006; Ouimet et al., 2009). Linear regression of log-slope versus log-area data yields the concavity and steepness indices (Wobus et al., 2006a). However, the fact that small changes in concavity correspond to large changes in steepness calls for the development of a normalized index. Sklar and Dietrich (1998) proposed a method for this normalization in which Equation 1 is evaluated using a reference slope ($S_r$) and a reference drainage area ($A_r$). By requiring the use of a single reference drainage area, this method does not allow for comparison of basins that differ in size, which is often crucial to these studies (e.g., Kirby et al., 2003). A second method involves regression of slope-area data using a reference concavity ($\theta_{ref}$) to find a normalized steepness index ($k_{sn}$) that allows for comparison of basins that vary in drainage area (Wobus et al., 2006a):

$$S = k_{sn} A^{-\theta_{ref}} \tag{2}$$

An additional consideration is the presence of knickpoints along the selected channels. Knickpoints represent a boundary (either migratory or stationary) between downstream sections

of a river profile that have adjusted to new conditions and upstream sections that have yet to adjust (e.g., Crosby and Whipple, 2006). Haviv et al. (2010) classified knickpoints into two groups: vertical-step and slope-break (Figure 10), both of which are visible as changes in gradient on slope-area plots (e.g., Wobus et al., 2006a). Although both categories of knickpoints can be mobile or stationary, Kirby and Whipple (2012) note that vertical-step knickpoints are often stationary, and often represent discrete changes along the profile (e.g., in lithology) rather than overarching tectonic influences. Slope-break knickpoints, in contrast, often migrate upstream at predictable rates and represent perturbations due to tectonic forcing, which makes them a key component in the study of tectonically active landscapes (e.g., Kirby et al., 2003).

## Methods

The goal of this study was to assess the robustness of geomorphic metrics and the DBPR landscape model in a more complex geologic setting. Following Hilley and Arrowsmith (2008), I evaluated basin relief, basin width, drainage area, normalized channel steepness, channel concavity, landslide density, and hillslope gradient in 17 basins along the left restraining bend of the SAF in the SCM using a 10m digital elevation model (DEM) in ESRI's ArcGIS software and a suite of MATLAB scripts. I extrapolated uplift rates from coastal marine terraces using data from Lajoie et al. (1979), Anderson (1990), and Weber and Allwardt (2001) (Figure 11). Projection of uplift rates from the coastal terraces is further justified by the fact that similar uplift rates were obtained from apatite fission track dating (Bürgmann et al., 1994) and $^{10}$Be dating (Perg et al., 2001; Gudmundsdottir et al., 2013). For the space-for-time substitution, I used slip rates of 15 – 18 mm/yr (d'Alessio et al., 2005) and found that each kilometer along the study

section of the SAF represents 56 – 67 k.y. of movement along the SAF. Uplift rates begin to decrease at 37 km along the study section of the SAF, which represents 2.1 – 2.5 m.y.

*Channel Analysis*

I selected 17 basins on the southwestern side of the SAF, each with a drainage area on the order of $10^5 – 10^7$ $m^2$. After delineating watershed boundaries in ArcMap using the DEM, I calculated basin relief by differencing the highest and lowest elevations in each basin. Following Hilley and Arrowsmith (2008), I measured average basin width parallel to the SAF; for each basin, I averaged multiple width measurements taken at 1000m increments (all parallel to the SAF; Figure 12A).

I extracted longitudinal channel profiles in order to map knickpoints, calculated normalized channel steepness indices ($k_{sn}$), and determined channel concavity ($\theta$) for each stream segment using Stream Profiler – a set of ArcMap tools and MATLAB scripts originally developed by Noah Snyder and Kelin Whipple (available at http://www.geomorphtools.org). Stream Profiler offers automated, batch, and manual processing options for evaluation of channel profiles (only a DEM is required; no premade GIS stream data sets are needed because Stream Profiler creates these outputs). The automated method calculates steepness indices along all streams in a DEM above a specified minimum drainage area. In batch processing, users select multiple channel heads to process at once. MATLAB extracts stream profiles downstream of the selected channel heads and calculates a normalized steepness index at each point along the stream. I only used batch processing as a reconnaissance tool at the onset of my study. Because batch processing

includes all sections of the stream (such as colluvial areas near the headwaters), includes knickpoints in steepness calculations, and averages steepness over small windows (which may yield erroneous steepness values due to the inherent scatter of slope-area plots), I manually evaluated the streams within my study area for the main analyses.

In manual selection, users work with individual channels and use log-log slope-area plots to manually define regression limits over which normalized steepness indices are calculated. Initial parameters are specified before channels can be selected. For this project, I selected spike removal and step removal for USGS 10 m DEMs, and left all other parameters as the default values. As mentioned above, abrupt decreases in slope at drainage areas of ~$10^6$ $m^2$ mark the transition from colluvial channels to fluvial channels (Montgomery and Foufoula-Georgiou, 1993; Figure 9), although debris flows may make this transition gradual (e.g., Stock and Dietrich, 2003). As a result, I limited my analysis to fluvial reaches defined by this break in slope. Only five channels were sufficiently segmented in their respective fluvial sections to merit a second (downstream) regression; therefore, I did not use these values to determine the final patterns of steepness and concavity. Steepness indices are normalized to a reference concavity ($\theta_{ref}$), which allows for comparison of gradients in basins with differing drainage areas (e.g., Kirby et al., 2003). Following Hilley and Arrowsmith (2008), I use a mean concavity of 0.81, evaluated in all undisturbed basins (i.e., those without knickpoints), as $\theta_{ref}$.This value falls outside the range of typical concavity values (0.4 – 0.6); this is likely due to variations in lithology, uplift rate, or climate along individual channels.

*Hillslope Analysis*

The metrics I used to evaluate hillslope response to uplift included average basin slope and landslide density (number of landslides per $km^2$), similar to Hilley and Arrowsmith (2008). I calculated average basin slope for all 17 drainages in ArcGIS and plotted this against distance along the SAF (from the restraining bend site northward).

I located landslides in ArcMap using aerial imagery and by identifying areas with scarps and hummocky or rough terrain. Due to the lack of available LiDAR data, I conducted this survey using the 10m DEM at a scale of 1:24,000 (to match the DEM). I used the landslide inventory from the Department of Conservation, California Geological Survey (http://maps.conservation.ca.gov/cgs/lsi/), for comparison. The inventory includes a greater number of landslides than my study, which reflects the limitation of a low resolution DEM and the subsequent restriction of this analysis to landslides large enough to be seen on the DEM. The lower resolution of the 10m DEM and the larger scale of my study area prevented analysis of landslide scar density. Thus, in order to facilitate comparison with the results of Hilley and Arrowsmith (2008), I counted the number of landslides in the study area. Rather than count the number of landslides per basin (which would skew the results due to varying basin sizes), I instead divided the study area evenly into eighteen 4km x 20km polygons and counted the number of landslides in each (Figure 12B).

## Results

I this section, I describe the patterns exhibited by geomorphic metrics calculated for 17 basins located southwest of the SAF (Figure 13). Relief gradually increases through the bend, drops after the maximum uplift, and increases gradually through the remainder of the study area. Average basin width and drainage area display nearly identical patterns (i.e., basins with the largest drainage areas also have the highest average widths); both metrics reach their peak within the bend and remain steady at all other locations, with the exception of one stream at the beginning of the study section. I confirm the quality of regression fits of log-log slope-area plots using $R^2$ values, which vary from 0.54 – 1.00 and average at 0.81 (Table 1, Appendix A). Concavity varies between 0.3 and 1.3 along the SAF; it peaks just before the uplift zone, and again at the end of the study section. The steepness index varies from 660 – 20,700, and experiences one peak of 18,800 at 36.7 km and again at 60.6 km (with a value of 20,700). Both of these peaks coincide with increasing uplift rates. Hillslope gradient and the number of landslides both increase gradually with distance NW along the SAF. Landslide occurrence notably increases northwest of the bend, peaking at 11 landslides ~11km past the bend (Figure 14).

Knickpoints are present on all but four channels studied (13 total channels with knickpoints; Figure 15). The number of knickpoints observed in each of these channels varies from 1–4. I take the uppermost boundary of each knickpoint to represent the maximum extent of perturbation along the channel, since knickpoint propagation represents the translation of disturbance through the channel network (lower panel, Figure 15). I classify knickpoints along seven of the thirteen

channels studied as the slope-break type (all others being more discrete, vertical step types). I find that the elevation of knickpoints increases with distance NW along the SAF; this trend is especially prevalent among those classified as slope-break (Figure 15).

## Discussion

A majority of the geomorphic metrics presented here follow patterns in the wake of the high uplift zone that are similar to those observed by Hilley and Arrowsmith (2008) in the DBPR. The positive scaling of average basin width with drainage area is intuitive, although several basins are oriented more parallel to the SAF and thus skew these results. These trends also align logically with basin relief, which increases through the restraining bend as channels incise following uplift. The largest number of landslides occurs just after the zone of high uplift, where relief and slope are highest. Most notably, steepness index tracks uplift within the restraining bend. These trends are consistent with expectations set in the DBPR.

Hilley and Arrowsmith (2008) use the peak in concavity that they observe to mark the end of channel response. The absence of such a peak here (the peak in concavity instead occurs before the uplift zone), makes it difficult to replicate their calculations of channel response time. However, the peak in concavity observed in the DBPR coincided with a peak in basin relief, which is present in the SCM. Thus, I instead use the peak in basin relief (at 41 km or 224 – 268 k.y. since the peak in uplift rates) to represent the end of channel response to uplift along the SAF restraining bend. The peak in identified landslides is past the northwestern end of the bend;

it is likely that the return of hillslopes to diffusive processes takes place beyond the study section. For the purposes of comparison, I use the end of the study section (75 km or 2.1 – 2.5 m.y. since the peak in uplift rates) to represent the end of hillslope response. Thus, there is an order of magnitude disparity between river and hillslope response of at least 1.9 m.y. This compares favorably to the results of Hilley and Arrowsmith (2008), who also found that hillslope response took an order of magnitude longer than that of channels (6.6 k.y. for channels versus 74 k.y. for hillslopes). However, due to continued uplift along strike of the SAF and the larger scale of the SCM area, hillslopes in this study site may not return to diffusive processes (or even have started as diffusive outside of the fault bend). Instead, the SCM may be dominated by threshold landscape evolution (i.e., erosion occurs via landsliding). In essence, the SCM landscape is continually influenced by multiple sources of uplift (Figure 11) through time while the DBPR responds to a single point source of uplift (upper left-hand panel, Figure 2).

In addition to the disparate cumulative uplift patterns, there is a difference in slip rate between the two sites (15 – 18 mm/y in the SCM versus 32 – 35 mm/yr along the DBPR). Both of these dissimilarities affect the space-for-time substitution because drainages in the SCM are experiencing different slip rates along the SAF and are undergoing continued uplift. The space-for-time substitution in the SCM is still valuable because it shows how channels and hillslopes respond to an increase in uplift rate. However, due to these complications, a response to the cessation of uplift cannot be recorded in the landscape; therefore, this field site does not provide a complete picture of landscape evolution.

In the SCM, I observe knickpoints on a majority of the selected channels, and therefore address their significance here. Hilley and Arrowsmith (2008) do not discuss knickpoints along the DBPR, which suggests that either a) the DBPR was unaffected by knickpoint propagation (unlikely, since the DBPR evolved in response to a pulse of uplift), b) Hilley and Arrowsmith omitted this information or c) the DBPR is sufficiently small such that knickpoints propagated rapidly before the study was conducted. In any case, the presence of knickpoints in the SCM adds to the complexity of this area relative to the DBPR. Because knickpoints inherently indicate a state of transience, their presence also calls into question previous work that assumed steady-state conditions (e.g., Gudmundsdottir et al., 2013). Knickpoint elevations increase with distance NW along the SAF, which indicates that knickpoints on channels farther along the SAF have had more time to adjust to new base levels. The slope break knickpoints exhibit this trend especially well: nearly all of these knickpoints are currently located within the SAF itself, and are likely migratory perturbations due to increasing uplift. I find that it is difficult to discern the mechanisms behind the vertical step knickpoints. A more detailed look at underlying lithologies and crossing faults reveals that few (if any) of these knickpoints are lithologically or structurally controlled; the only observed lithologic changes in the vicinity of knickpoints are from sandstones to shales, and none of the knickpoints are bounded by faults. However, these vertical steps are small in height compared to the slope breaks (~20 m vertical steps versus sweeping ~100 m slope breaks); this may indicate that the controls are highly localized such that I cannot identify them remotely using these data. Possible influences may include local changes in lithology that are not detectable in ArcGIS or from previous mapping conducted at a large spatial scale, small landslides that cause local scale changes to channel morphology, and minor unmapped faults. Detailed and targeted fieldwork may provide concrete data on knickpoint

controls as well as on channel form in general, and should be considered a key component in future work.

In terms of the geomorphic metrics that I analyzed, one pattern stands out as vastly different from those observed in the DBPR. Values for the concavity index found in this study range from 0.31 to 2.2. These are high relative to the typical range, high relative to the DBPR values, and are more variable than expected. Only 4 of the 22 regressed channel segments have concavities that lie within the generally predicted steady state values (0.4 – 0.6). The concavity index is influenced by lithologic, climatic, and uplift rate variations along the length of the channel. While subtle differences in the sedimentary units detailed above may contribute to these high concavities, it is likely that climatic differences also play a role. Roe et al. (2002) explored the effects of variability in orographic precipitation on the concavity index in an effort to improve landscape evolution and erosion models. They found that different amounts of precipitation across mountain ranges exert significant control on the concavity index. In environments where prevailing winds push moisture to higher elevations, higher precipitation at the headwaters of streams provides increased erosive power, which leads to lower concavities. In contrast, when the prevailing winds are negligible, precipitation is concentrated in the lower sections of the channel profile, which leads to higher channel concavity in the lower reaches of streams. Bürgmann et al. (1994) note that precipitation patterns indeed vary across the SCM; average annual precipitation totals 30 – 35 cm/yr in San Jose, 100 cm/yr in Loma Prieta, and 50 – 76 cm/yr in Santa Cruz. Using these data, the SCM exhibit a climatic regime in which precipitation is concentrated at higher elevations. Based on the findings of Roe et al. (2002), the concavities should therefore be lower in the upper reaches of these streams. Although only five of the

studied channels required a second regression, all five exhibited higher concavity in their lower reaches. While precipitation definitely influences concavity, these findings still do not satisfactorily explain why concavity indices are outside of the generally accepted range. Ultimately, the high concavity can likely by explained by the combination of lithology and precipitation with the continued accrual of uplift discussed above. The cessation of uplift in the DBPR is a key component of the Hilley and Arrowsmith (2008) study that is not present in the SCM. While steepening of channels still occurs in both systems due to increased uplift rate, concavity does not display the same patterns without complete termination of uplift (i.e., the continued accumulation of uplift in the SCM prevents concavity from displaying a pattern similar to that observed along the DBPR).

While most of the geomorphic metrics studied by Hilley and Arrowsmith (2008) are robust in this more complex setting, the dissimilarity between the continuous uplift around the restraining bend and the pulse of uplift in the DBPR permits only a partial application of their results to the SCM. Specifically, the channels in the space-for-time substitution can still be viewed as developmental stages, but only record a response to the spike in uplift rates that occurs in the bend (i.e., a complete picture of channel evolution is not available, since uplift continues along the SAF). Additionally, the complexities of the SCM cannot be ignored despite the robustness of the metrics. The presence of knickpoints, for example, indicates that the landscape is in a transient stage; this goes hand in hand with the idea that the continuous uplift along the SAF does not allow the landscape to reach true equilibrium. Even partial observation of the DBPR results in the SAF, however, is significant to the future of tectonic geomorphology; as

methodology is improved over subsequent generations of study (including the added benefits of fieldwork), a greater understanding of the landscape using these metrics may be possible.

## Limitations & Future Work

Overall, the results presented here represent a thorough comparison of the SCM to the DBPR using remote analyses such as ArcGIS and MATLAB. However, several factors limited this work, and may be avoided in future projects in order to improve our understanding of landscape evolution. Lack of LiDAR coverage limited the accuracy and level of detail obtainable in identifying landslides; thus, I identified landslides using a 10 m DEM based on the presence of scarps and hummocky topography visible at a scale of 1:24000. This project lacked a field component. Future work may improve the accuracy of regressions by verifying the locations of different surface process domains; it may also aid in the identification of landslides, of lithologic and structural effects on the landscape, and of vegetative and climatic influences. This study is also limited by the programs and protocols used, including ArcMap and MATLAB, as well as by the Stream Profiler code. In the future, new codes such as TopoToolbox (available at https://topotoolbox.wordpress.com/download/) may be used to improve these analyses. Limitations aside, reevaluation of landscape evolution models in the context of increasingly complex geologic settings is an important next step in the advancement of tectonic geomorphology.

## Conclusions

The goal of this study was to evaluate the robustness of a landscape evolution model (from the DBPR) and its associated geomorphic metrics in a more complex setting (the SCM). I emulated the landmark study by Hilley and Arrowsmith (2008) and used ESRI's ArcGIS software and MATLAB to evaluate these geomorphic metrics in the SCM. Results of this study suggest that even in larger scale settings with more complex geology and varying climate, geomorphic metrics such as channel steepness index and basin relief remain useful tools for evaluating landscape evolution in response to uplift. The concavity index, however, exceeds generally accepted values (more so than the DBPR) and does not follow expected patterns through the restraining bend.

While these high concavities (relative to accepted values) do not appear to alter the trends of the other geomorphic metrics, they highlight a key aspect of this area that complicates the DBPR model. Specifically, the continued accrual of uplift (as opposed to the pulse of uplift in the DBPR), as well as along-channel variations in uplift rates and precipitation, prevents the complete application of the DBPR model to the SCM. The space-for-time substitution is still useful for examining changes in channel form in the wake of increased uplift rate, but does not record any response to the cessation of uplift (which does not occur). Presence of knickpoints in the studied channels indicates transience in the landscape, and calls into question studies of the SCM that assume steady-state. However, increasing elevation of slope-break knickpoints in basins northwest along the SAF aligns with expectations of channel response to perturbation

(i.e., that knickpoints to the northwest have propagated farther because they have had more time to respond).

Application of models to field settings is an important step in the advancement of tectonic geomorphology; future studies should further reapply these ideas in complex settings where LiDAR coverage exists, other data are readily available, and a fieldwork component is feasible. The addition of fieldwork to subsequent reiterations of this study as well as new studies in other areas will provide key information including checks on GIS data sets, on lithology, and on knickpoint characterization. Overall, this study shows that 1) it is possible to observe trends in the SCM similar to those of the DBPR and 2) uplift patterns, climate, and lithology are key confounding factors that should be accounted for when modeling mountain ranges.

## References


Anderson, R. S., 1990, Evolution of the northern Santa Cruz Mountains by advection of crust past a San Andreas fault bend, Science, 249, 397- 401.

Anderson, R. S., 1994, Evolution of the Santa Cruz Mountains, California, through tectonic growth and geomorphic decay: Journal of Geophysical Research, v. 99, p. 20161–20179, doi: 10.1029/94JB00713.

Aydin, A. and Page, B. M., 1984, Diverse Pliocene-Quaternary tectonics in a transform environment, San Francisco Bay region, California: Geological Society of America Bulletin, v. 95, p. 1303 – 1317.

Aydin, A., Johnson, A. M., and Fleming, R. W., 1992, Right-lateral-reverse surface rupture along the San Andreas and Sargent faults associated with the October 17, 1989, Loma Prieta, California, earthquake: Geology, v. 20, p. 1063, doi:10.1130/0091-7613(1992)020<1063:RLRSRA>2.3.CO;2.

Bradley, W. C. and Griggs, G. B., 1976, Form, genesis, and deformation of central California wave-cut platforms: Geological Society of America Bulletin, v. 87, p. 433, doi: 10.1130/0016-7606(1976)87<433:FGADOC>2.0.CO;2.

Burbank, D. W. and Anderson, R. S., 2001, Tectonic Geomorphology. Blackwell, Oxford.

Bürgmann, R., Arrowsmith, R., Dumitru, T., and McLaughlin, R., 1994, Rise and fall of the southern Santa Cruz Mountains, California, deduced from fission track dating, geomorphic analysis, and geodetic data: Journal of Geophysical Research, v. 99, p. 20,181–20,202, doi: 10.1029/94JB00131.

Clark, J. C. and J. D. Rietman, 1973, Oligocene stratigraphy, tectonics, and paleogeography southwest of the San Andreas fault, Santa Cruz Mountains and Gabilan Range, California Coast Ranges: U.S. Geol. Surv. Profess. Pap. 783, 18 pp.

Coppersmith, K. J., 1979, Activity assessment of the Zayante-Vergeles fault, central San Andreas fault system, central California [Ph.D. thesis]: Santa Cruz, University of California, 216 pp.

Crosby, B. T. and Whipple, K. X., 2006, Knickpoint initiation and distribution within fluvial networks: 236 waterfalls in the Waipaoa River, North Island, New Zealand: Geomorphology, v. 82, p. 16–38.

d'Alessio, M. A., Johanson, I. A., Bürgmann, R., Schmidt, D. A., and Murray, M. H., 2005, Slicing up the San Francisco Bay Area: Block kinematics and fault slip rates from GPS-derived surface velocities: Journal of Geophysical Research, v. 110, p. B06403, doi: 10.1029/2004JB003496.

DiBiase, R. A., Whipple, K. X., Heimsath, A. M., and Ouimet, W. B., 2010, Landscape form and millennial erosion rates in the San Gabriel Mountains, CA: Earth and Planetary Science Letters, v. 289, p. 134–144, doi: 10.1016/j.epsl.2009.10.036.

Duvall, A., Kirby, E., and Burbank, D., 2004, Tectonic and lithologic controls on bedrock channel profiles and processes in coastal California. J. Geophys. Res., v. 109, p. F03002, doi: 10.1029/2003JF000086.

Fernandes, N. F. and Dietrich, W. E., 1997, Hillslope evolution by diffusive processes; the timescale for equilibrium adjustments: Water Resources Research, v. 33, p. 1307–1318, doi: 10.1029/97WR00534.

Flint, J. J., 1974, Stream gradient as a function of order, magnitude, and discharge: Water Resources Research, v. 10, p. 969–973, doi: 10.1029/WR010i005p00969.

Graymer, R. W., Moring, B. C., Saucedo, G. J., Wentworth, C. M., Brabb, E. E., and Knudsen, K. L., 2006b, Geologic map of the San Francisco Bay region: U.S. Geological Survey Scientific Investigations Map 2918, http://pubs.usgs.gov/sim/2006/2918.

Gudmundsdottir, M. H., Blisniuk K., Ebert Y., Levine N. M., Rood D.H., Wilson A., and Hilley G. E., 2013, Restraining bend tectonics in the Santa Cruz Mountains, California, imaged using $^{10}$Be concentrations in river sands: Geology, v. 41, p. 843–846. doi: 10.1130/G33970.1.

Hack, J. T., 1957, Studies of longitudinal stream profiles in Virginia and Maryland: U.S. Geological Survey Professional Paper 294-B, p. 97.

Hack, J. T., 1973, Stream-profile analysis and stream-gradient index: Journal of Research of the U. S. Geological Survey, v. 1, p. 421–429.

Haviv, I., Enzel, Y., Whipple, K. X., Zilberman, E., Matmon, A., Stone, J., and Fifield, K. L., 2010, Evolution of vertical knickpoints (waterfalls) with resistant caprock: insights from numerical modeling: J. Geophys. Res., v. 115, p. F03028.

Heimsath, A. M., Dietrich, W. E., Nishiizumi, K., and Finkel, R. C., 1997, The soil production function and landscape equilibrium: Nature, v. 388, p. 358–361, doi: 10.1038/41056.

Hilley, G. E. and Arrowsmith, J. R., 2008, Geomorphic response to uplift along the Dragon's Back pressure ridge, Carrizo Plain, California: Geology, v. 36, p. 367–370, doi:10.1130/G24517A.1.

Howard, A. D., 1994, A detachment-limited model of drainage basin evolution: Water Resources Research, v. 30, p. 2261–2285, doi: 10.1029/94WR00757.

Kirby, E., Whipple, K. X., 2001, Quantifying differential rock-uplift rates via stream profile analysis: Geology, v. 29, p. 415–418.

Kirby, E., Whipple, K. X., Tang, W. and Zhiliang, C., 2003, Distribution of active rock uplift along the eastern margin of the Tibetan Plateau: Inferences from bedrock channel longitudinal profiles, J. Geophys. Res., v. 108, no. B4, 2217, doi: 10.1029/2001JB000861.

Kirby, E. and Whipple, K. X., 2012, Expression of active tectonics in erosional landscapes: Journal of Structural Geology, v. 44, p. 54–75, doi: 10.1016/j.jsg.2012.07.009.

Lague, D., Crave, A., and Davy, P., 2003, Laboratory experiments simulating the geomorphic response to tectonic uplift: Journal of Geophysical Research, v. 108, doi: 10.1029/2002JB001785.

Lajoie, K. R., Weber, G. E., Mathieson, S., and Wallace, J., 1979, Quaternary tectonics of coastal Santa Cruz and San Mateo Counties, California, as indicated by deformed marine terraces and alluvial deposits: Coastal Tectonics and Coastal Geologic Hazards in Santa Cruz and San Mateo Counties, California: A Field Trip Guide: Geological Society of America, Cordilleran Section, p. 61–82.

McLaughlin, R. J., Clark, J. C., and Brabb, E. E., 1988, Geologic map and structure sections of the Loma Prieta 7 1/2' quadrangle, Santa Clara and Santa Cruz Counties, California, U.S. Geol. Surv. Open File Map, 88-752.

Montgomery, D. R. and Foufoula-Georgiou, E., 1993, Channel network representation using digital elevation models: Water Resources Research, v. 29, p. 3925–3934, doi: 10.1029/93WR02463.

Ouimet, W. B., Whipple, K. X., and Granger, D. E., 2009, Beyond threshold hillslopes: channel adjustment to base-level fall in tectonically active mountain ranges. Geology 37, 579–582, doi: 10.1130/G30013A.1.

Quaternary Fault and Fold Database of the United States: http://earthquake.usgs.gov/hazards/qfaults/ (accessed April 2016).

Roe, G. H., Montgomery, D. R., and Hallet, B., 2002, Effects of orographic precipitation variations on the concavity of steady-state river profiles: Geology (Boulder), v. 30, p. 143–146.

Schwartz, S. Y., D. L. Orange, and R. S. Anderson, 1990, Complex fault interactions in a restraining bend on the San Andreas Fault, southern Santa Cruz Mountains, California: Geophys. Res. Lett. v. 17, p. 1207-1210.

Sklar, L. S. and Dietrich, W. E., 1998, River longitudinal profiles and bedrock incision models: stream power and the influence of sediment supply. In: Tinkler, K. J. and Wohl, E. E.

(Eds.), Rivers over Rock: Fluvial Processes in Bedrock Channels, AGU Press, Washington, D. C., p. 237–260.

Sklar, L. S. and Dietrich, W. E., 2006, The role of sediment in controlling steady-state bedrock channel slope: implications of the saltation-abrasion incision model: Geomorphology, v. 82, p. 58–83.

Snyder, N. P., Whipple, K. X., Tucker, G. E., and Merritts, D. J., 2000, Landscape response to tectonic forcing: Digital elevation model analysis of stream profiles in the Mendocino triple junction region, northern California: Geological Society of America Bulletin, v. 112, p.1250–1263, doi: 10.1130/0016–7606(2000)112<1250:LRTTFD>2.3.CO;2.

Stock, J. D. and Dietrich, W. E., 2003, Valley incision by debris flows: Evidence of a topographic signature, Water Resour. Res., v. 39, no. 4, 1089, doi: 10.1029/2001WR001057.

Tucker, G. E. and Slingerland, R., 1997, Drainage basin response to climate change: Water Resources Research, v. 33, p. 2031–2047, doi: 10.1029/97WR00409.

Tucker, G. E., 2004, Drainage basin sensitivity to tectonic and climatic forcing: Implications of a stochastic model for the role of entrainment and erosion thresholds: Earth Surface Processes and Landforms, v. 29, p. 185–205, doi:10.1002/esp.1020.

Tucker, G. E. and G. R. Hancock, 2010, Modelling landscape evolution: Earth Surface Processes Landforms, v. 35, p. 28–50, doi:10.1002/esp.1952.

Valensise, G. and Ward, S. N., 1991, Long-term uplift of the Santa Cruz coastline in response to repeated earthquake along the San Andreas fault, Bull. Seismol. Soc. Am., 96, 1694-1704.

van der Beek, P. and Braun, J., 1998, Numerical modeling of landscape evolution on geological time-scales: A parameter analysis and comparison with the southeastern highlands of Australia: Basin Research, v. 10, p.49–68, doi: 10.1046/j.1365–2117.1998.00056.x.

Weber, G. E. and Allwardt, A. O., 2001, The geology from Santa Cruz to Point Año Nuevo: The San Gregorio fault zone and Pleistocene marine terraces: U.S. Geological Survey Bulletin, v. 2188, p. 1–32.

Whipple, K. X. and Tucker, G. E., 1999, Dynamics of the stream-power river incision model: Implications for height limits of mountain ranges, landscape response timescales, and research needs: Journal of Geophysical Research, ser. B, Solid Earth and Planets, v. 104, p. 17,661–17,674, doi: 10.1029/1999JB900120.

Willett, S. D., and Brandon, M. T., 2002, On steady states in mountain belts: Geology, v. 30, p. 175, doi: 10.1130/0091-7613(2002)030<0175:OSSIMB>2.0.CO;2.

Willgoose, G., Bras, R. L., and Rodriguez-Iturbe, I., 1991, A coupled channel network growth and hillslope evolution model. 1: Theory: Water Resources Research, v. 27, p.1671–1684, doi: 10.1029/91WR00935.

Wobus, C., Whipple, K. X., Kirby, E., Snyder, N., Johnson, J., Spyropoulou, K., Crosby, B., and Sheehan, D., 2006a, Tectonics from topography: procedures, promise, and pitfalls. Geol. Soc. Am. Spec. Pap. 398, 55–74, doi: 10.1130/2006.2398(04).

## Figures

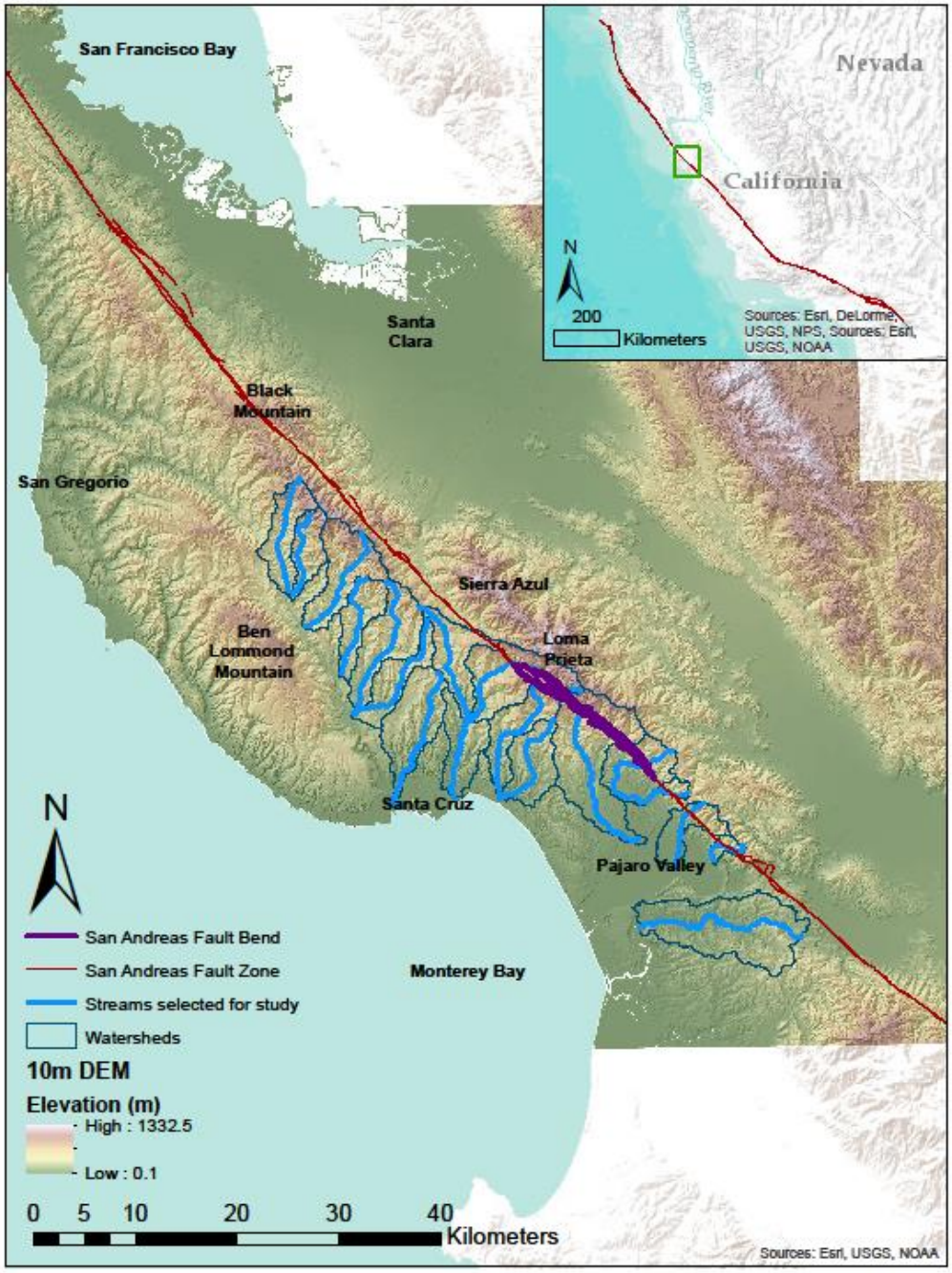


**Figure 1.** Study area map showing selected streams (in light blue) and watersheds (in dark blue), the San Andreas Fault (in red), and the restraining bend (in purple) underlain by the 10m DEM used in this study. Inset map shows location within California, USA (outlined in green) along with the SAF (in red).

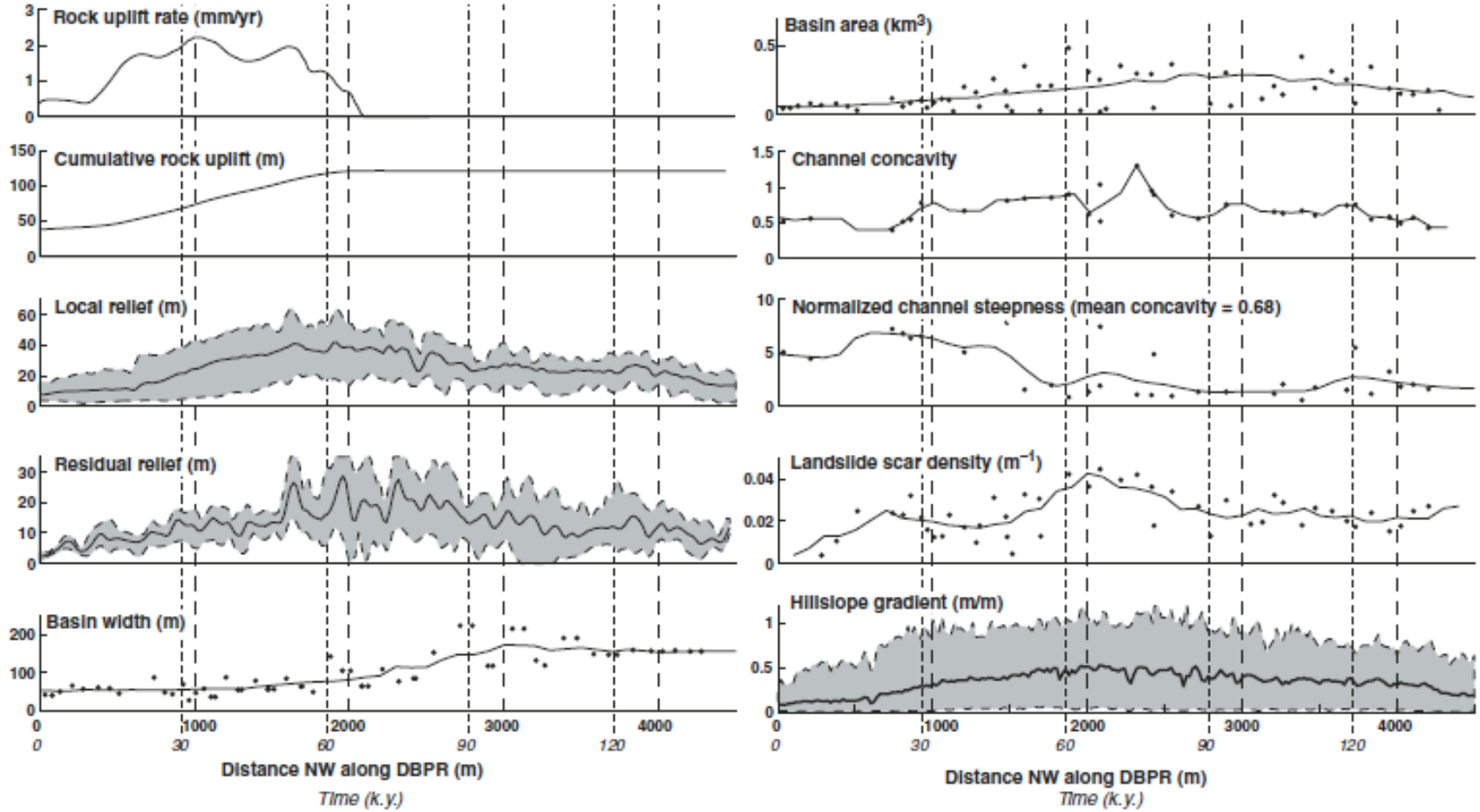


**Figure 2.** Results taken from Hilley and Arrowsmith (2008) showing how their geomorphic metrics changed throughout the DBPR. Note that the x-axes display distance along the DBPR as well as time in k.y., indicating use of the space-for-time substitution. Solid lines indicate 500 m running averages. For local relief, residual relief, and hillslope gradient, the solid line represents the mean value while the gray region represents the 95% error bounds. Uplift ceases around the 2.1 km mark. Channel response continues until the 2.3 km mark, where concavity peaks, while hillslope response continues until the 4 km mark where diffusive processes return.

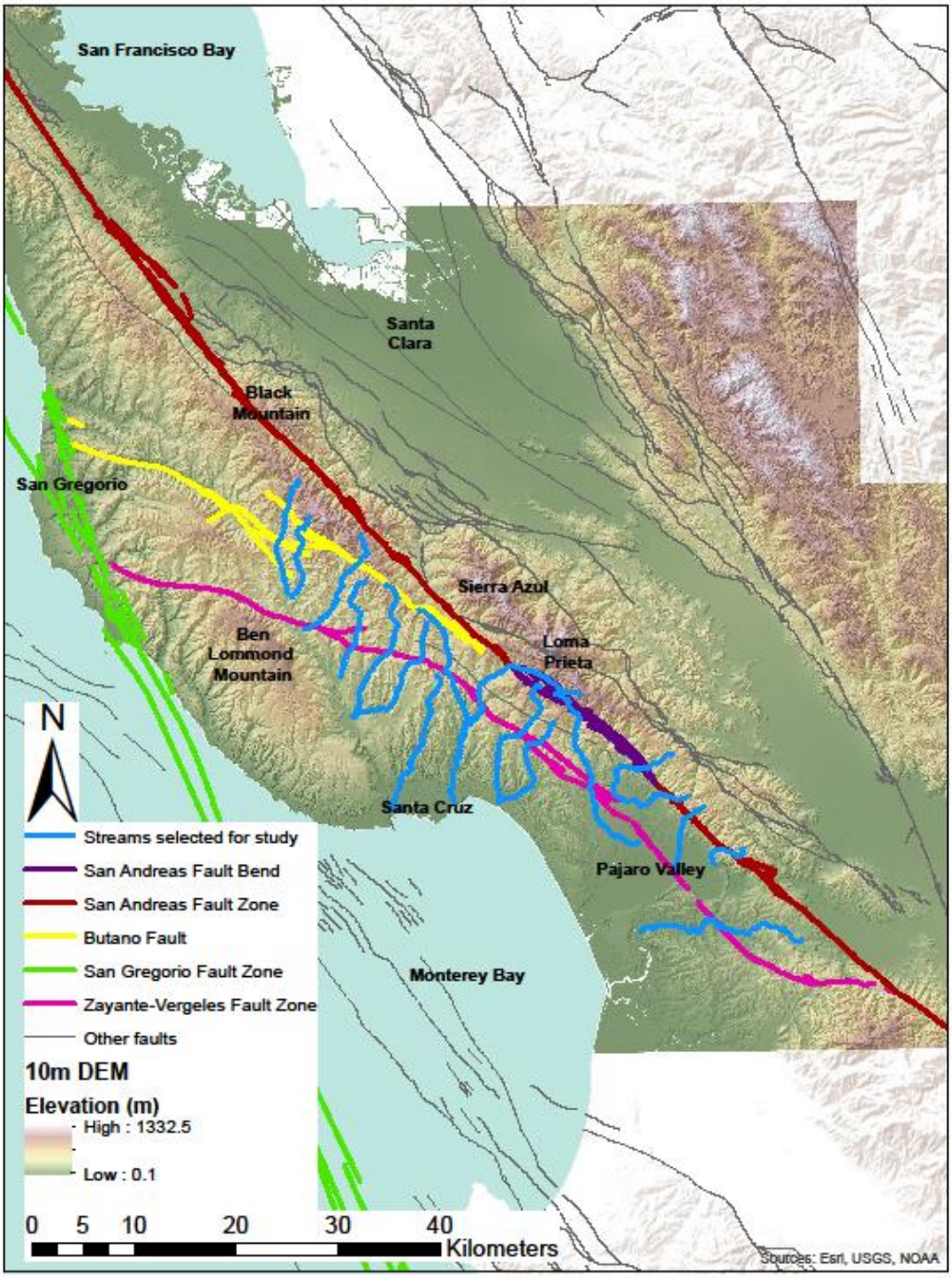


**Figure 3.** Map showing relevant structures in addition to the SAF that lie within the study area, including the San Gregorio Fault (green), the Butano Fault (yellow), and the Zayante-Vergeles Fault Zone (pink). The San Andreas Fault is in red, with the restraining bend highlighted in purple. Other faults are shown in gray, and illustrate the complex nature of this area.

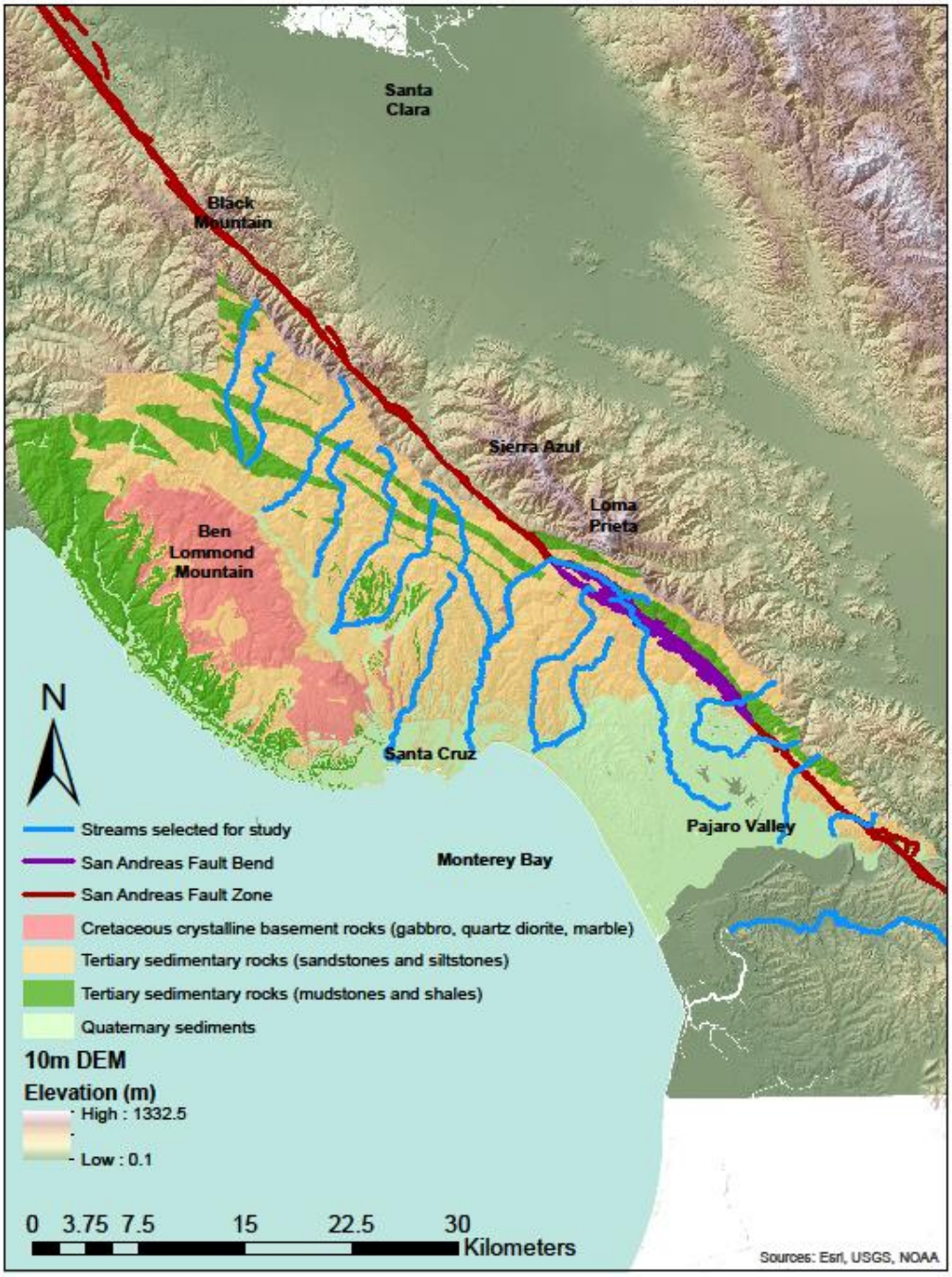


**Figure 4.** Map showing generalized lithology of the study area. Harder, crystalline basement rocks (red) are limited to Ben Lommond Mountain. Sedimentary rocks cover the rest of the study area; harder sandstones and siltstones are shown in orange, softer mudstones and shales are in dark green. Low-lying areas such as Pajaro Valley are filled with Quaternary sediments (light green).

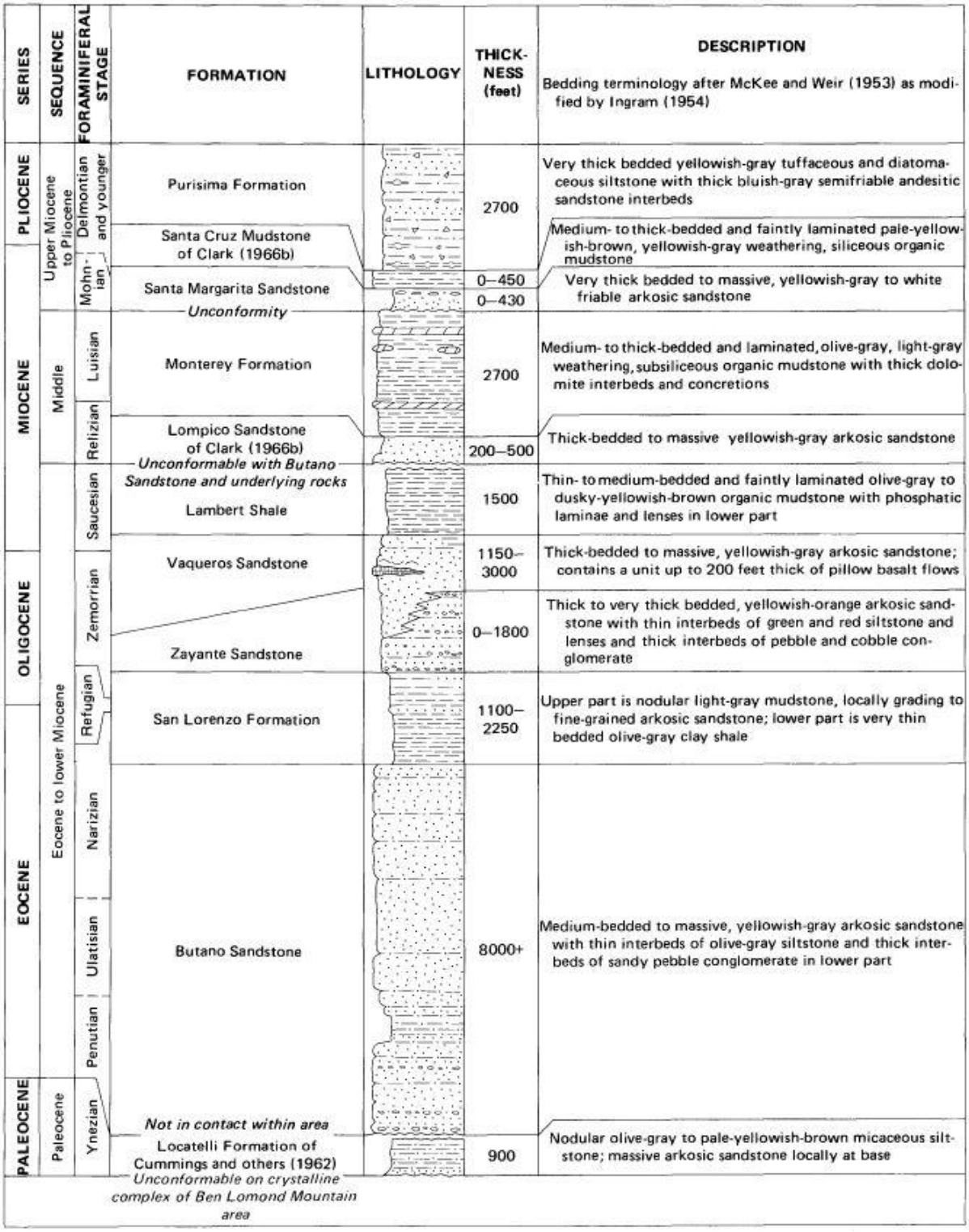


**Figure 5.** Stratigraphy of Tertiary sedimentary units that cover most of the study area. Figure taken from Clark and Rietman (1973).

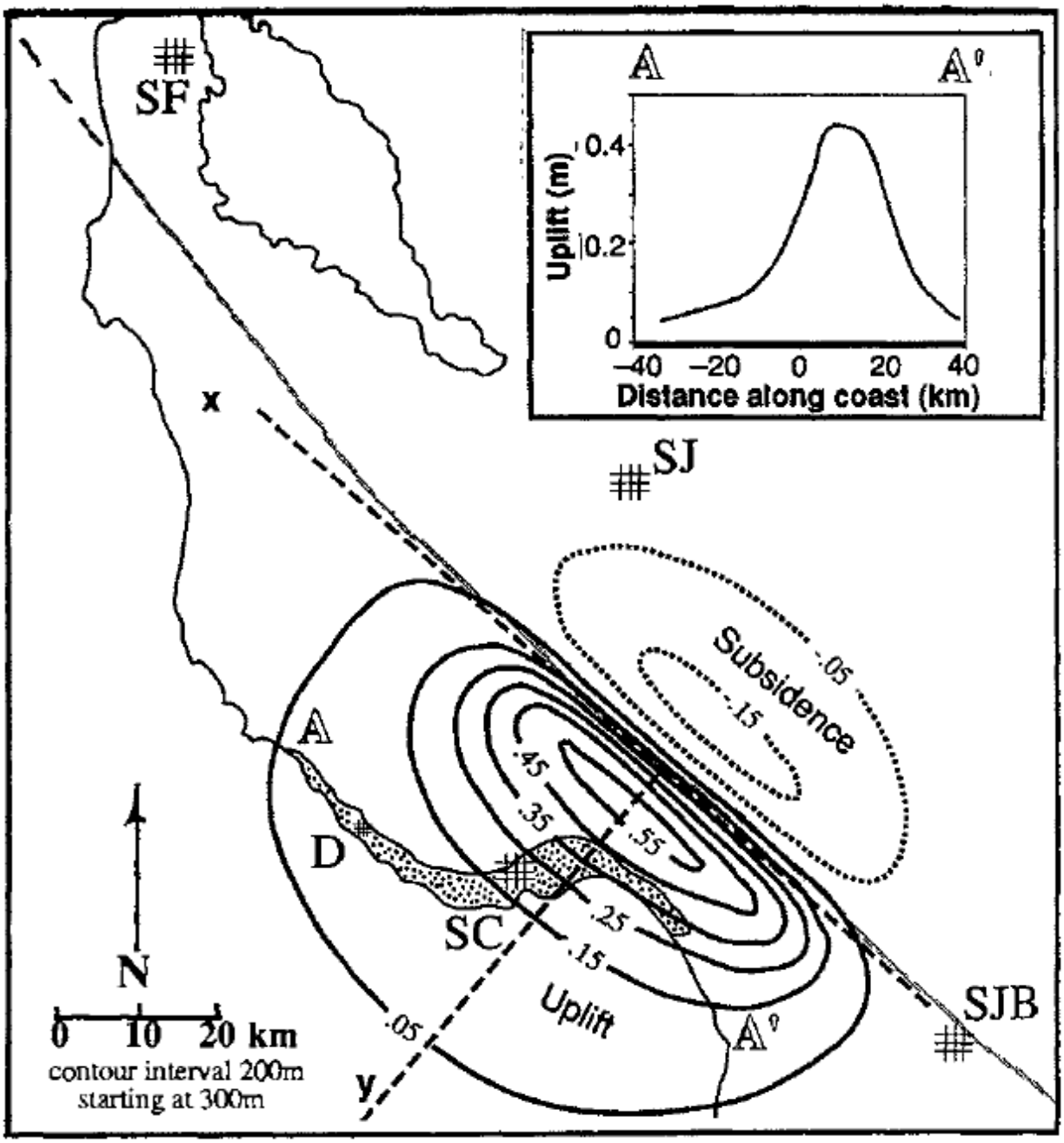


**Figure 6.** Map of uplift contours (in meters) taken from Anderson (1990). Note the slight subsidence northeast of the SAF. The shaded area along the coast represents marine terraces. The inset shows predicted uplift along transect A-A,' which traverses the coastline.

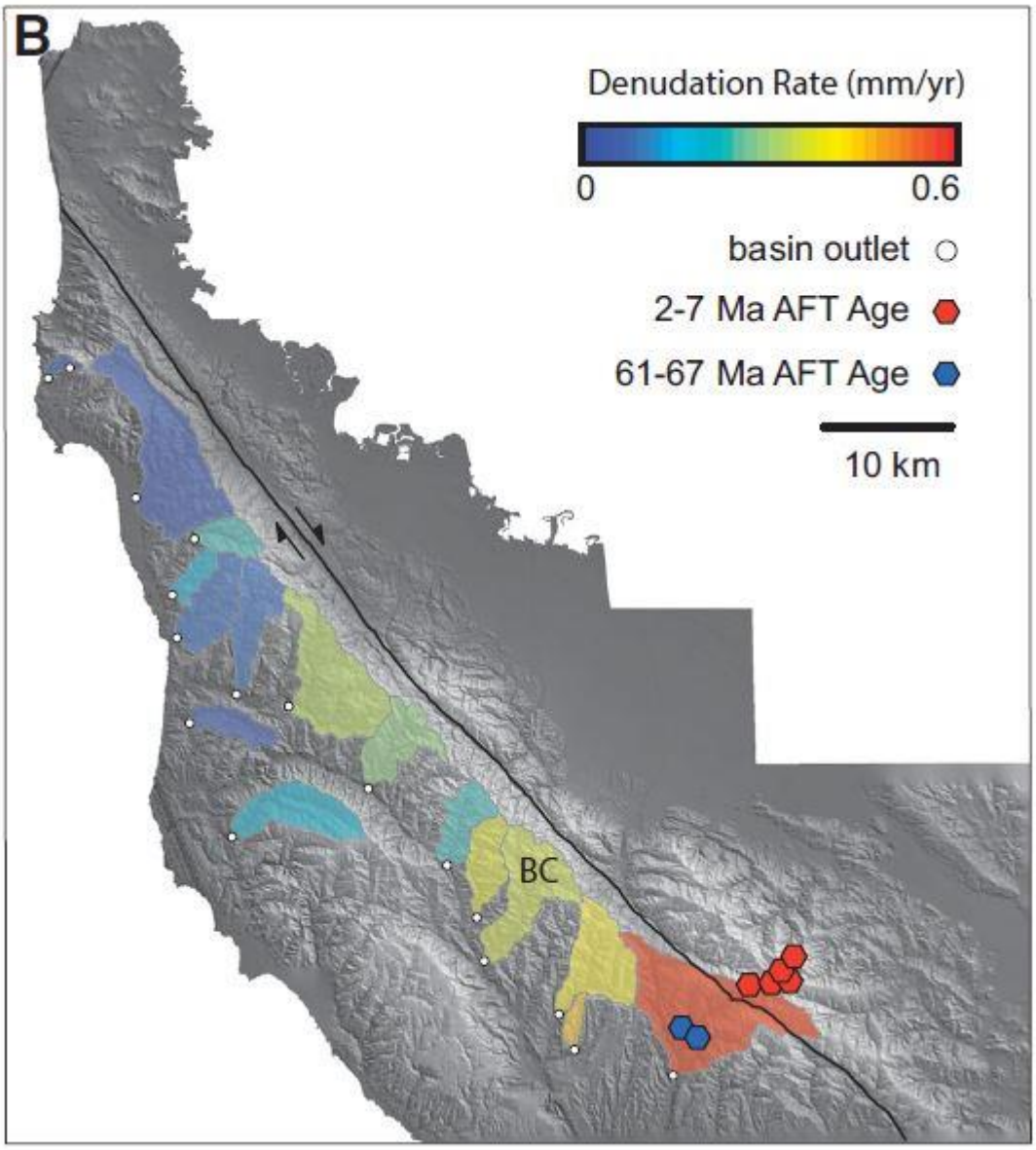


**Figure 7.** Map showing drainage basins studied by Gudmundsdottir et al. (2013) and apatite fission track data from Bürgmann et al. (1994). Warmer colored drainage basins represent those with higher denudation rates (and by proxy higher uplift rates). Red hexagons represent apatite fission track samples that were reset in the Cenozoic; blue hexagons represent apatite fission track samples that were reset in the Mesozoic. Figure taken from Gudmundsdottir et al. (2013).

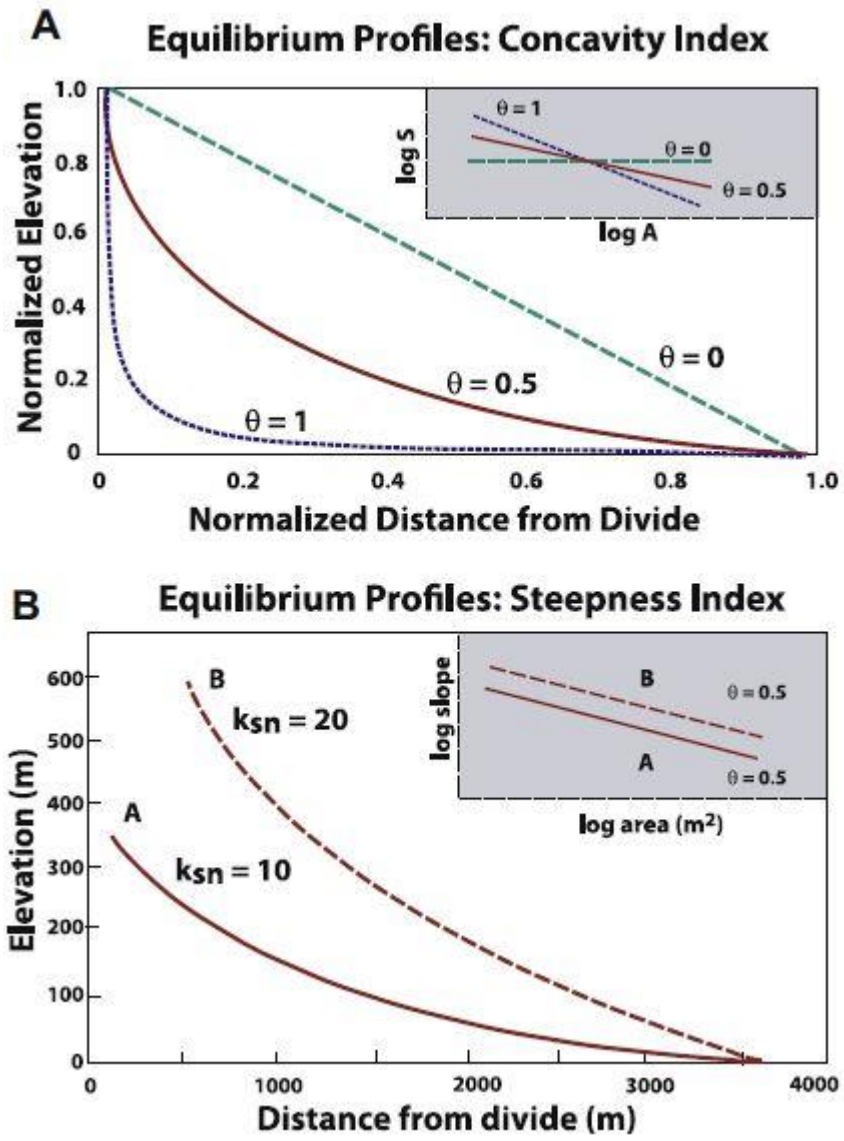


**Figure 8.** Diagram showing relationships of concavity and steepness on channel profiles. Insets show concavity on log-log slope-area plots. (A) Illustration of how concavity changes with profile shape. (B) Depiction of two channels with different steepness but same concavity. Adapted from Kirby and Whipple (2012); originally modified from Duvall et al. (2004) and Whipple and Tucker (1999).

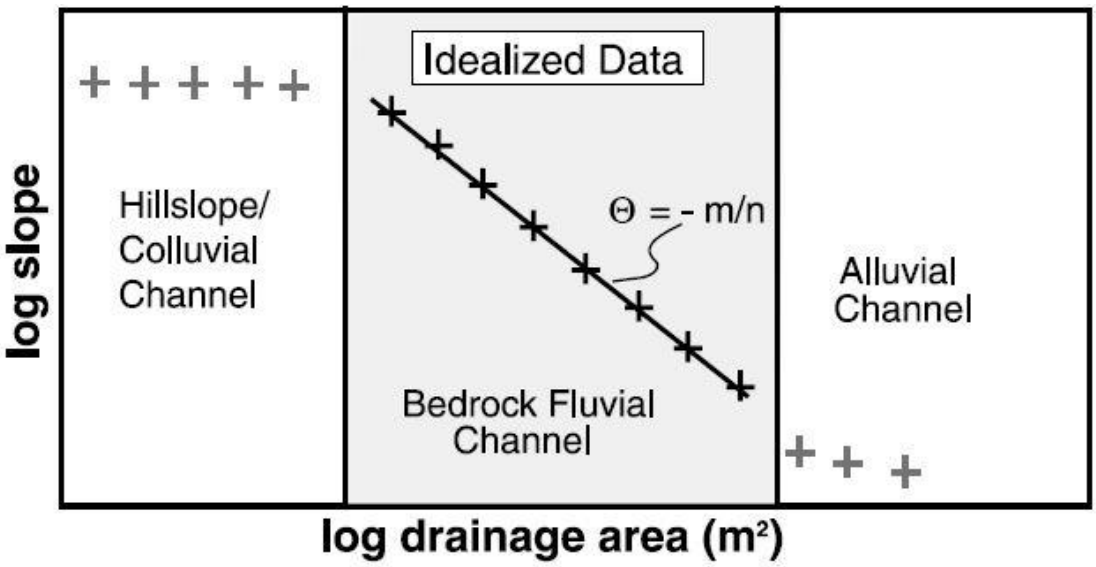


**Figure 9.** Idealized log slope – log area profile, showing the breaks in slope indicative of changes from colluvial to fluvial to alluvial channels. Figure taken from Duvall et al. (2004).

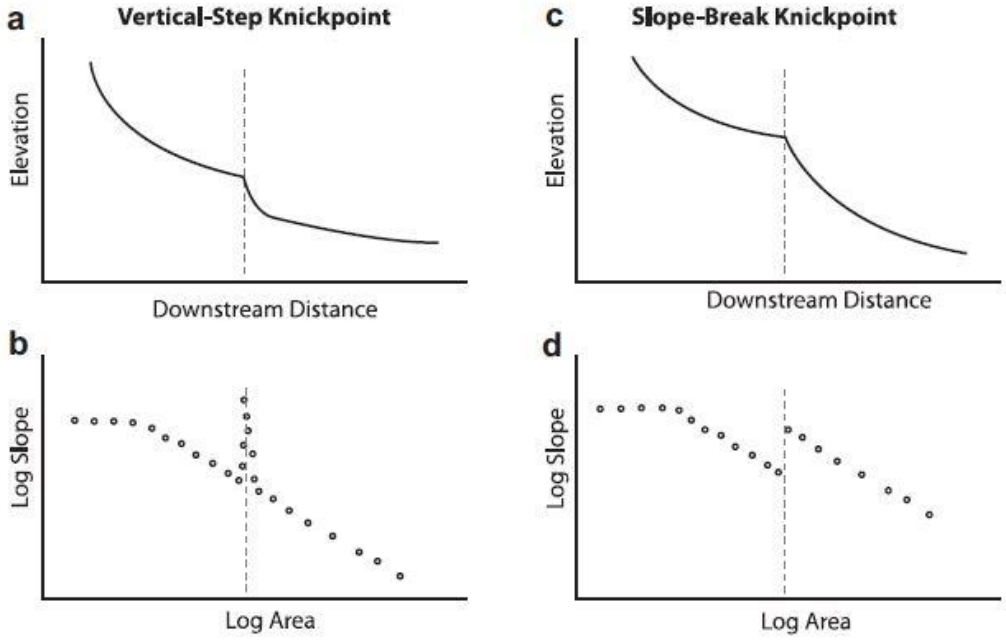


**Figure 10.** Diagram showing the two different classifications of knickpoints on longitudinal profiles (a and c), as well as on log-log plots of slope versus drainage area (b and d). Figure taken from Kirby and Whipple (2012).

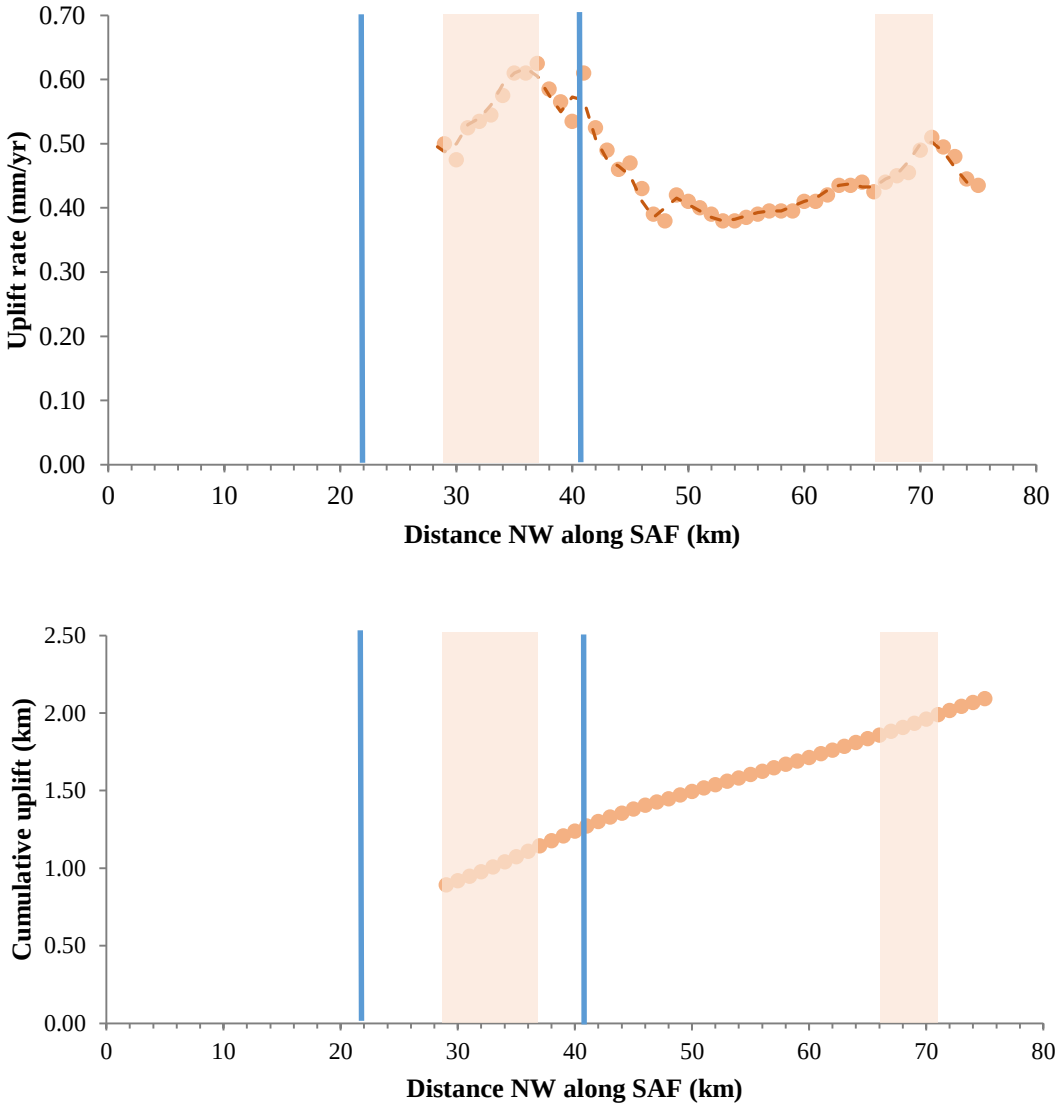


**Figure 11.** (Left) Plot of uplift rates in the Santa Cruz Mountains extrapolated inland from the coastal marine terraces. Uplift rates are not available in the first 30 km of study section along the San Andreas Fault. Direction of Pacific Plate motion is to the right. The dashed line is a two-point running average. (Right) Cumulative uplift calculated using a space-for-time substitution. The initial uplift (preceding the study section) is not known; thus an initial value was calculated by assuming a constant uplift over the first 30 km. Blue lines indicate the beginning and end of the bend, and the pale red shaded areas highlight areas of sharply increasing uplift rate. The second pulse of uplift (at 68 – 71 km) is possibly associated with the San Gregorio Fault Zone.

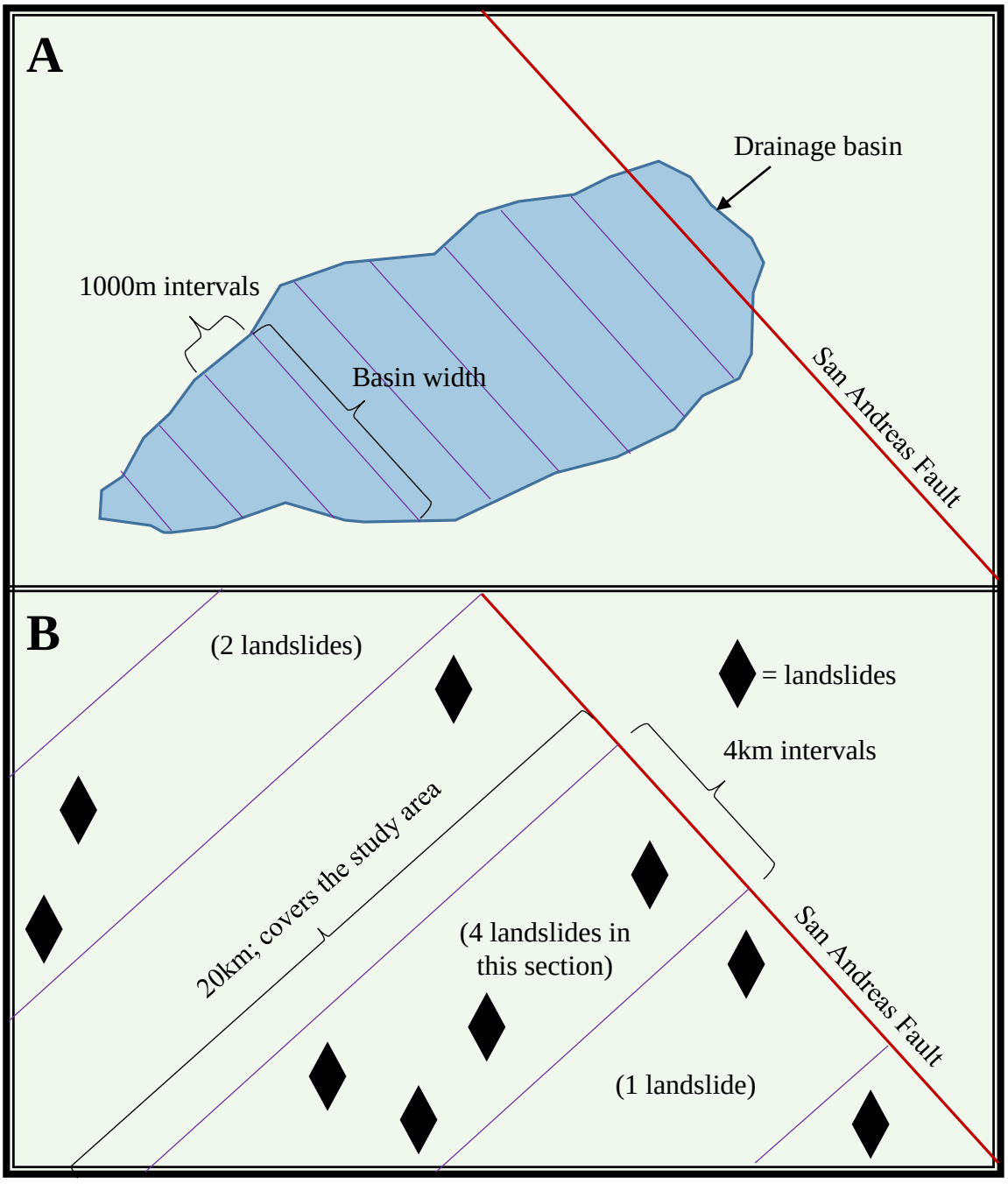


**Figure 12.** Diagram showing (A) how basin width was calculated and (B) how the number of landslides was counted. The red line represents the San Andreas Fault in both (A) and (B). I measured multiple basin widths (purple lines in A) for each drainage basin at 1000m intervals and then averaged these values. I divided the study area into eighteen 4km x 20km sections (purple lines in B) and counted the number of landslides (diamonds) in each.

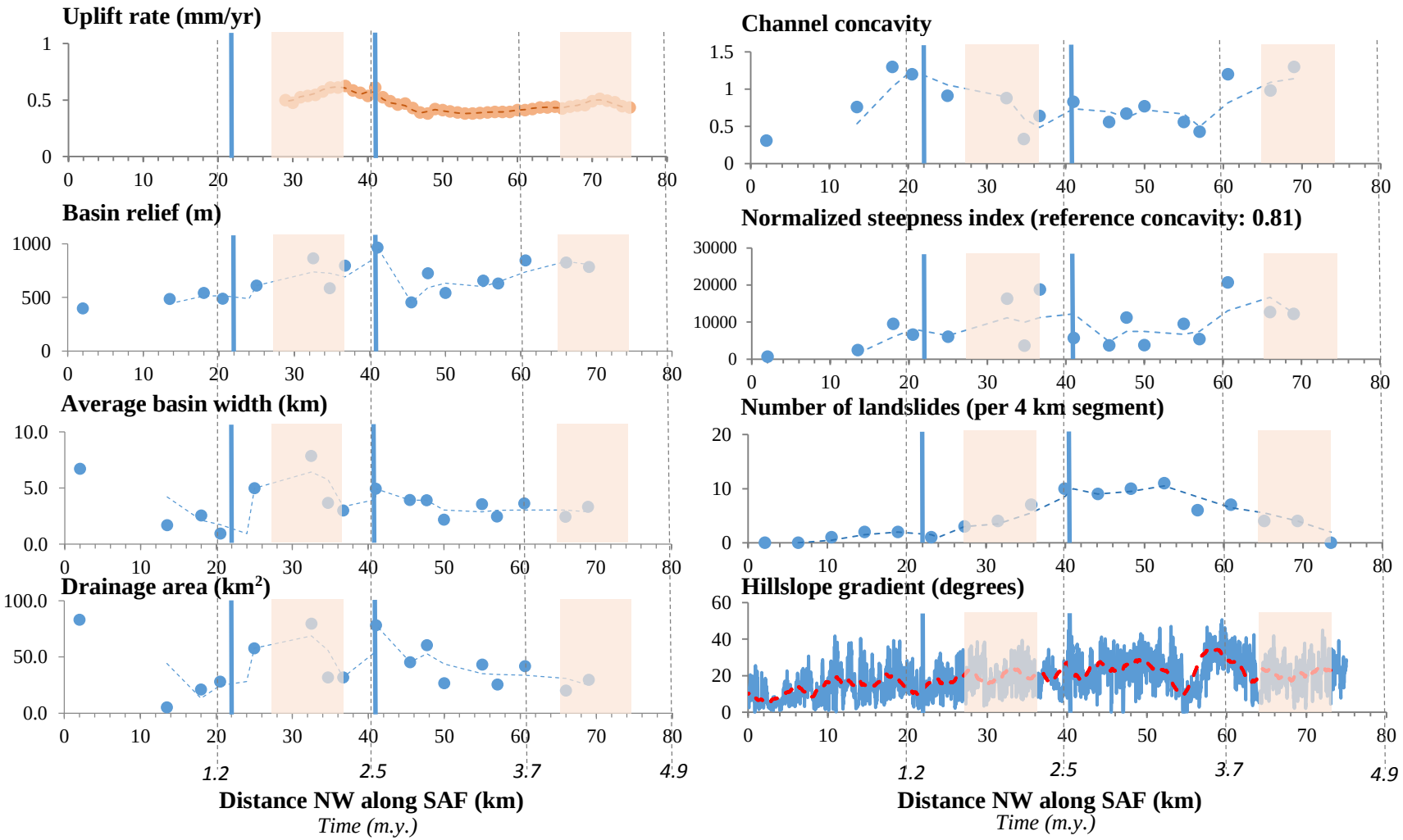


**Figure 13.** Summary of geomorphic metric results along the SAF. Pacific plate movement is to the right (NW). Data points represent values for a single stream (17 total in each plot), while the dashed lines show 2-point running averages. Solid blue vertical lines represent the boundaries of the restraining bend; pale red shaded areas correspond to increasing uplift rates as shown in the upper left-hand panel. The uplift to the far right is thought to be caused by the San Gregorio fault zone. In addition to distance, the x-axis shows the time substitution (italicized) in millions of years.

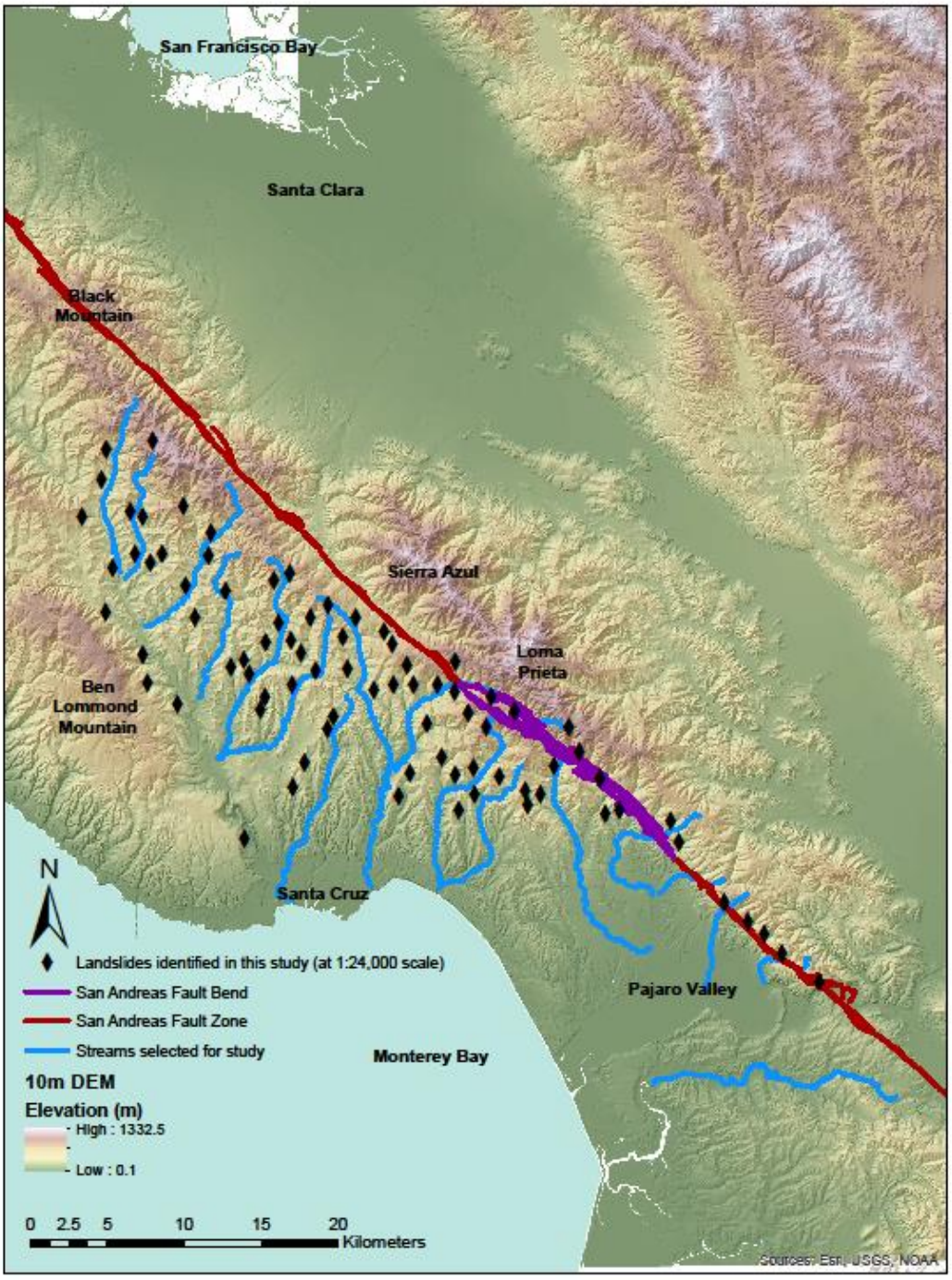


**Figure 14.** Map detailing the locations of landslides identified in this study (black diamonds), based on hummocky topography, scarps, and evidence from aerial imagery. This analysis was conducted at a scale of 1:24000 to match the DEM; therefore, landslides mapped here are limited to those with features noticeable at this scale. Studied streams are in blue and the SAF is in red.

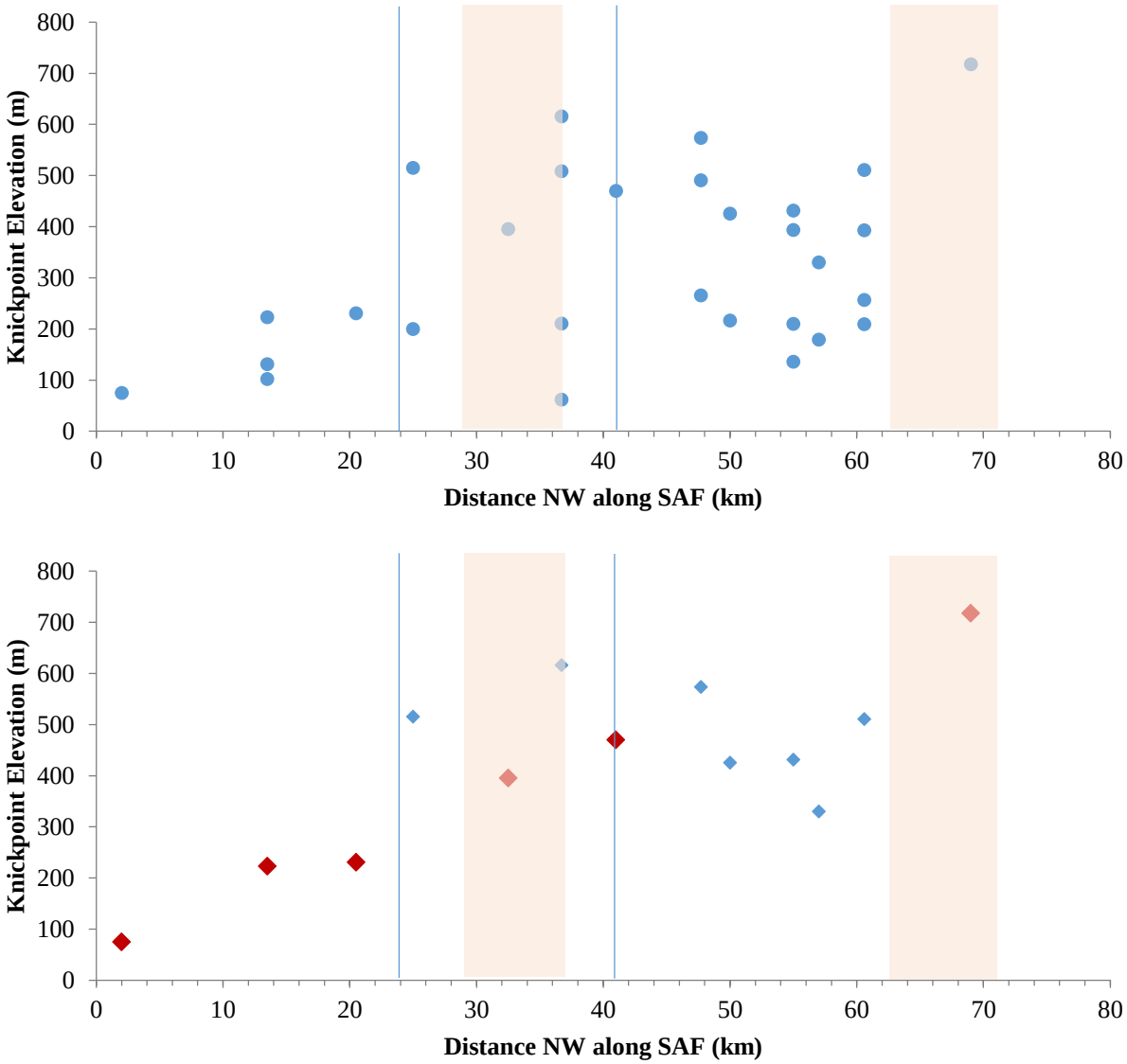


**Figure 15.** Plots of knickpoint elevation with increasing distance NW along the SAF. Solid blue lines represent the boundaries of the restraining bend; pale red shaded areas correspond to zones exhibiting increasing uplift rates. The upper panel shows all knickpoints observed, regardless of type or position along the channel. Vertical alignments of points indicate that a given channel contains multiple knickpoints. The bottom panel shows only the uppermost knickpoint, taken to represent the farthest extent of perturbation. The red diamonds indicate that the knickpoint type is slope-break, whereas all others are discrete, vertical step knickpoints. Note that knickpoints in channels to the left of the plots, which have presumably had the most time to evolve since passing through the bend, are farther up the channel.

## Tables

**Table 1.** Summary of geomorphic metric results along the SAF. Five streams required multiple regressions due to segmentation of the fluvial section of the profile. Values for R2 indicate quality of fit of regression limits on slope-area plots. Single asterisks mark channels that cross the SAF; double asterisks mark channels that run parallel to the SAF at their headwaters.

| Stream # | Stream Name | Distance NW along SAF (km) | $k_{sn}$ | $\theta$ | $R^2$ | Basin relief (m) | Average basin width (km) | Drainage area ($km^2$) | Number of landslides | Average basin hillslope gradient (degrees) |
|---|---|---|---|---|---|---|---|---|---|---|
| 1 | Elkhorn Slough | 2 | 656 | 0.31 | 1.00 | 398.8 | 6.7 | 83.3 | 1 | 11.4 |
| | | 2 | 5700 | 0.86 | 0.88 | - | - | - | - | - |
| 2 | Mattos Gulch* | 13.5 | 2430 | 0.76 | 0.75 | 486.1 | 1.7 | 5.20 | 1 | 17.6 |
| | | 13.5 | 6410 | 2.2 | 0.82 | - | - | - | - | - |
| 3 | Coward Creek* | 18 | 9520 | 1.3 | 0.84 | 541.3 | 2.6 | 21.3 | 3 | 11.7 |
| 4 | Hughes Creek* | 20.5 | 6650 | 1.2 | 0.93 | 488.9 | 0.9 | 28.2 | 0 | 18.5 |
| | BEND STARTS | 24 | | | | | | | | |
| 5 | Green Valley Creek* | 25 | 6070 | 0.91 | 0.90 | 611.5 | 5.0 | 57.9 | 4 | 13.5 |
| 6 | Corralitos Creek** | 32.5 | 16300 | 0.88 | 0.86 | 864.2 | 7.9 | 79.7 | 7 | 15.4 |
| 7 | Valencia Creek | 34.7 | 3640 | 0.33 | 0.59 | 586.1 | 3.7 | 31.9 | 3 | 15.2 |
| | | 34.7 | 6380 | 0.94 | 0.62 | - | - | - | - | - |
| 8 | Aptos Creek** | 36.7 | 18800 | 0.64 | 0.54 | 797.2 | 3.0 | 31.8 | 4 | 20.4 |
| 9 | Soquel Creek* | 41 | 5700 | 0.83 | 0.93 | 965.9 | 4.9 | 78.3 | 12 | 21.3 |
| | | 41 | 27800 | 1.3 | 0.86 | - | - | - | - | - |
| | BEND ENDS | 41 | | | | | | | | |
| 10 | Branciforte Creek | 45.5 | 3700 | 0.56 | 0.86 | 455.0 | 3.9 | 45.3 | 5 | 15.8 |
| 11 | West Branch Soquel Creek | 47.7 | 11200 | 0.67 | 0.81 | 725.0 | 3.9 | 60.6 | 7 | 18.7 |
| 12 | Bean Creek | 50 | 3820 | 0.77 | 0.85 | 541.8 | 2.2 | 26.8 | 4 | 17.3 |
| | | 50 | 6510 | 1.1 | 0.90 | - | - | - | - | - |
| 13 | Zayante Creek | 55 | 9520 | 0.56 | 0.71 | 658.1 | 3.6 | 43.3 | 10 | 19.5 |
| 14 | Newell Creek | 57 | 5430 | 0.43 | 0.69 | 631.2 | 2.5 | 25.7 | 4 | 21.3 |
| 15 | Shear Creek | 60.6 | 20700 | 1.2 | 0.85 | 846.1 | 3.6 | 42.0 | 8 | 22.9 |
| 16 | Kings Creek | 66 | 12700 | 0.98 | 0.76 | 826.5 | 2.5 | 20.1 | 3 | 22.4 |
| 17 | San Lorenzo River | 69 | 12200 | 1.3 | 0.85 | 784.9 | 3.3 | 29.9 | 5 | 20 |

# Appendices

*Appendix A: Logarithmic Slope-Area Plots*

Raw logarithmic slope-area plots generated from analysis of the 17 channels using ArcMap and MATLAB (Stream Profiler tools). I present these data in order of increasing distance NW of the SAF (as is done in the figures above). Each plot includes 3 subplots: elevation versus distance (top), drainage area versus distance (middle), and slope versus drainage area (bottom). Raw channel data is in green, step-removed data is in pink, natural concavity fits are in blue, and forced reference concavity fits are in turquoise. For slope area plots, crosshairs represent raw data while red squares represent log-bin averages of slope-area data.

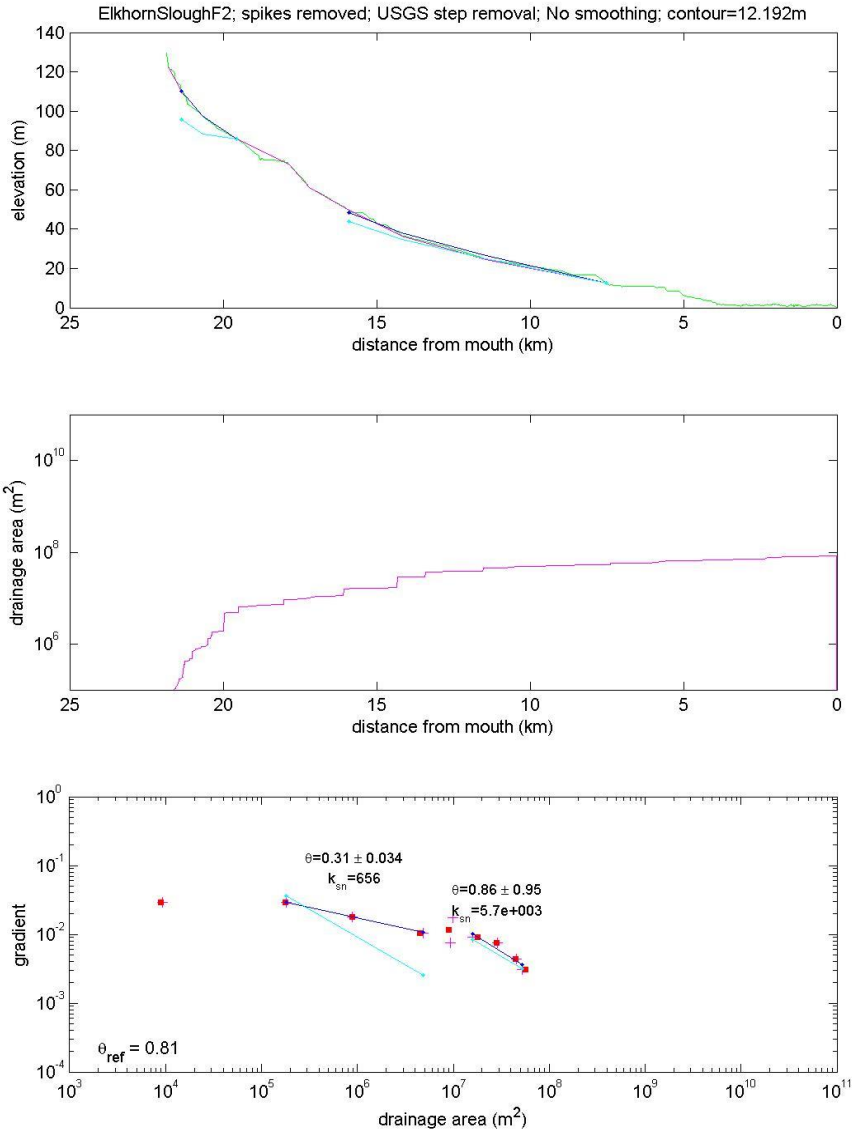

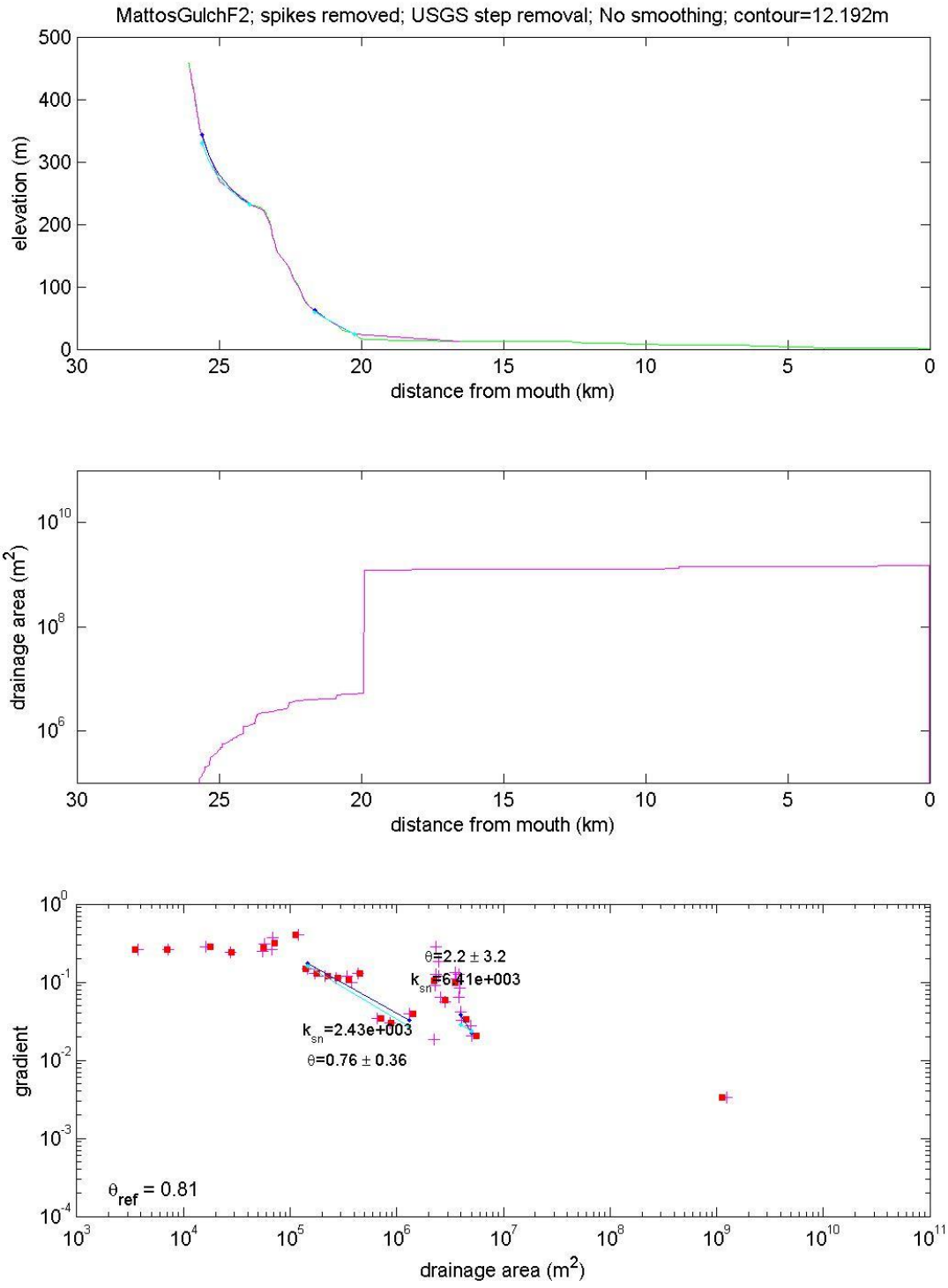
MattosGulchF2; spikes removed; USGS step removal; No smoothing; contour=12.192m
elevation (m)
distance from mouth (km)
drainage area (m2)
distance from mouth (km)
gradient
θ=2.2 ± 3.2
ksn=6.41e+003
ksn=2.43e+003
θ=0.76 ± 0.36
θref = 0.81
drainage area (m2)

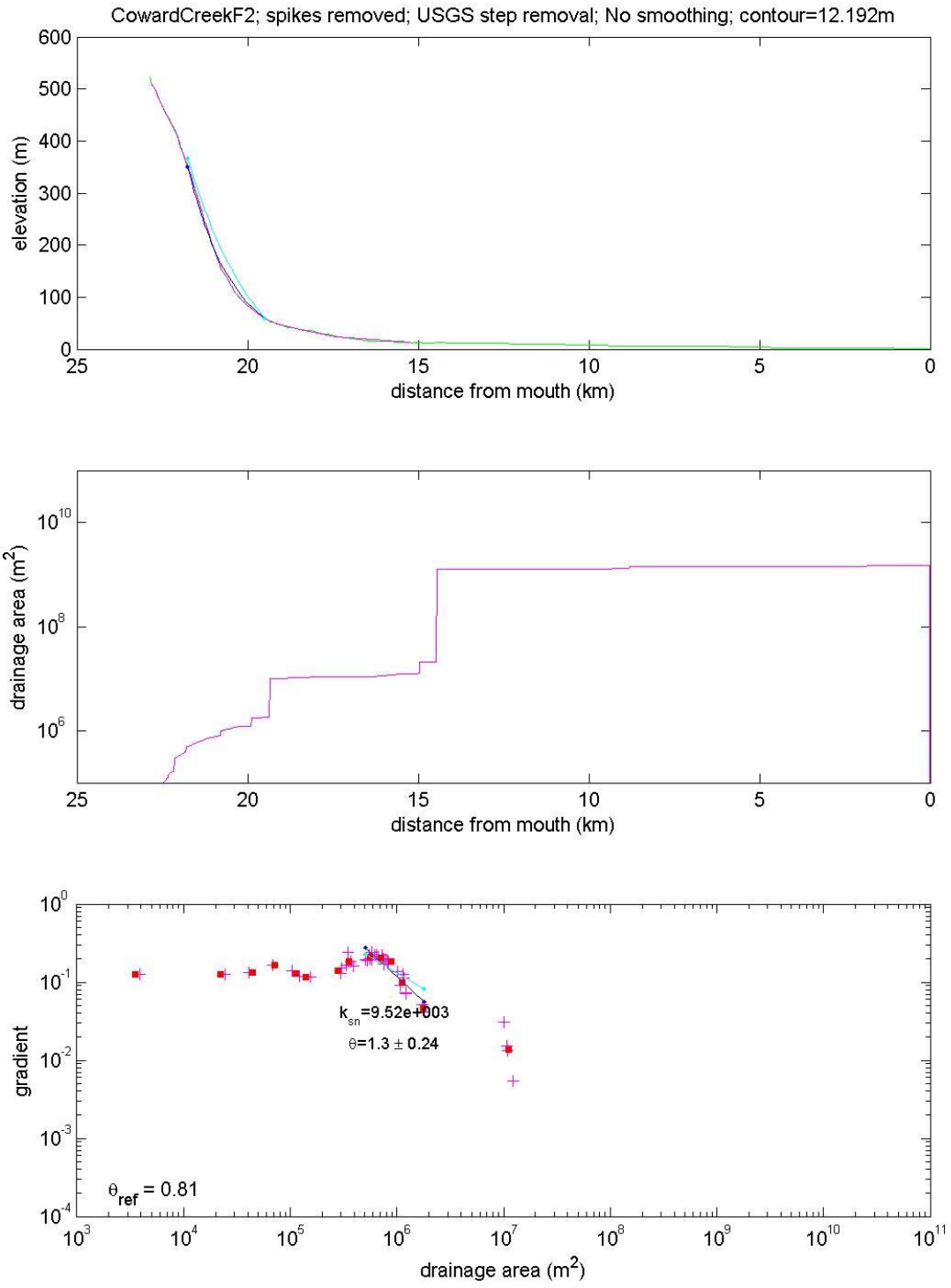
CowardCreekF2; spikes removed; USGS step removal; No smoothing; contour=12.192m
elevation (m)
distance from mouth (km)
drainage area (m2)
distance from mouth (km)
gradient
ksn=9.52e+003
θ=1.3 ± 0.24
θref = 0.81
drainage area (m2)

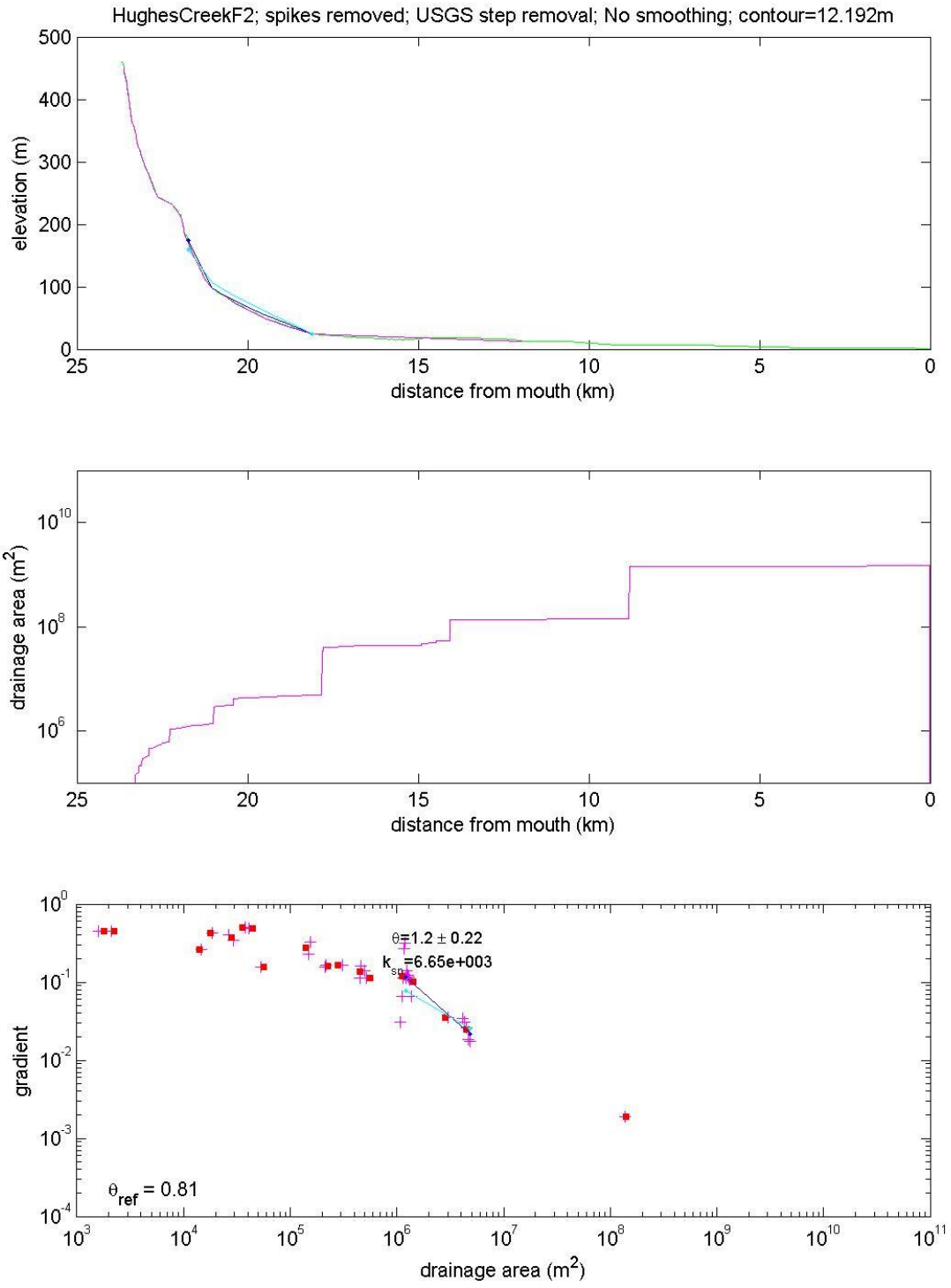
HughesCreekF2; spikes removed; USGS step removal; No smoothing; contour=12.192m
elevation (m)
distance from mouth (km)
drainage area (m2)
distance from mouth (km)
gradient
θ=1.2 ± 0.22
ksn=6.65e+003
θref = 0.81
drainage area (m2)

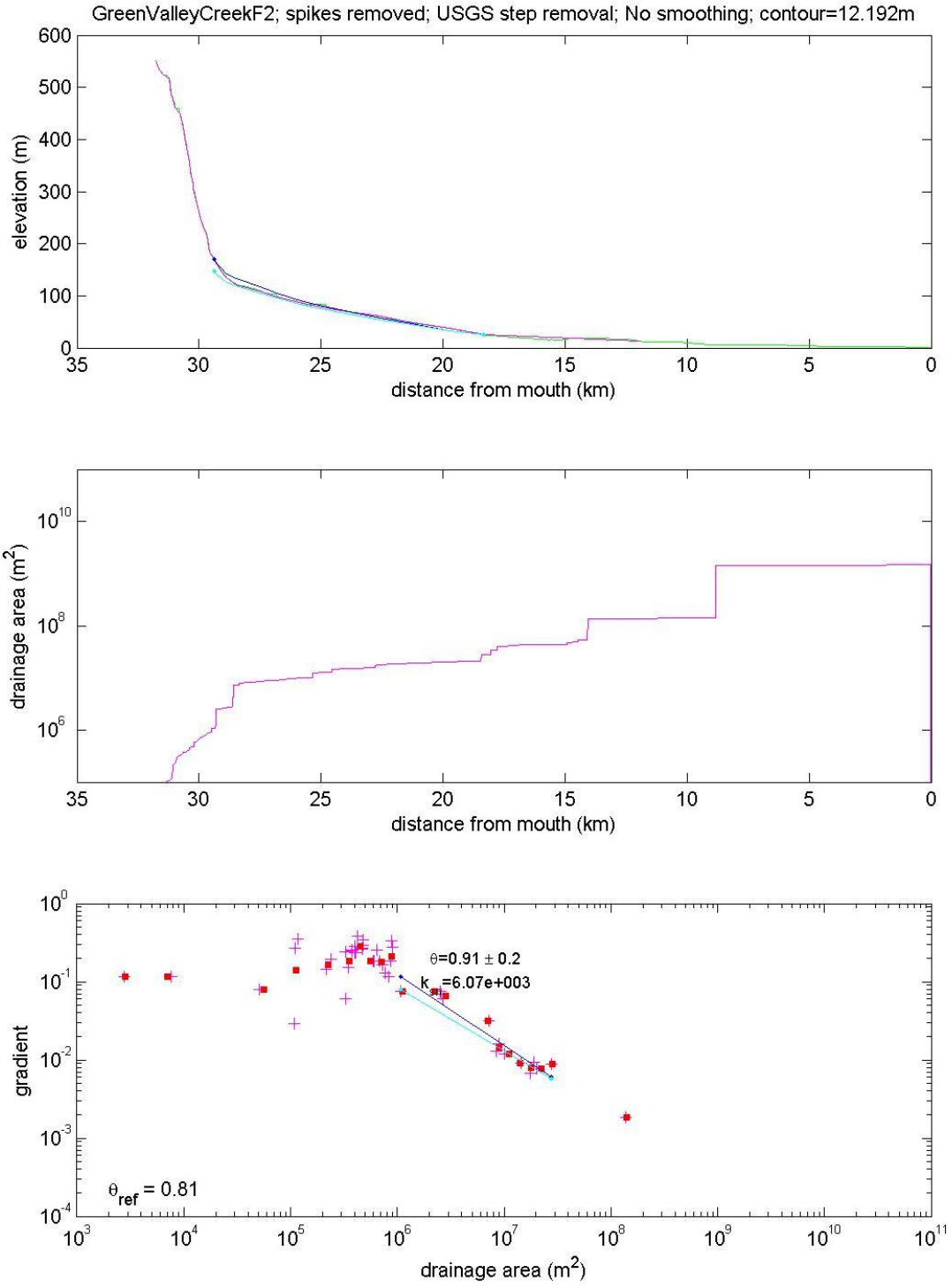
GreenValleyCreekF2; spikes removed; USGS step removal; No smoothing; contour=12.192m
elevation (m)
distance from mouth (km)
drainage area (m2)
distance from mouth (km)
gradient
θ=0.91 ± 0.2
k =6.07e+003
θref = 0.81
drainage area (m2)

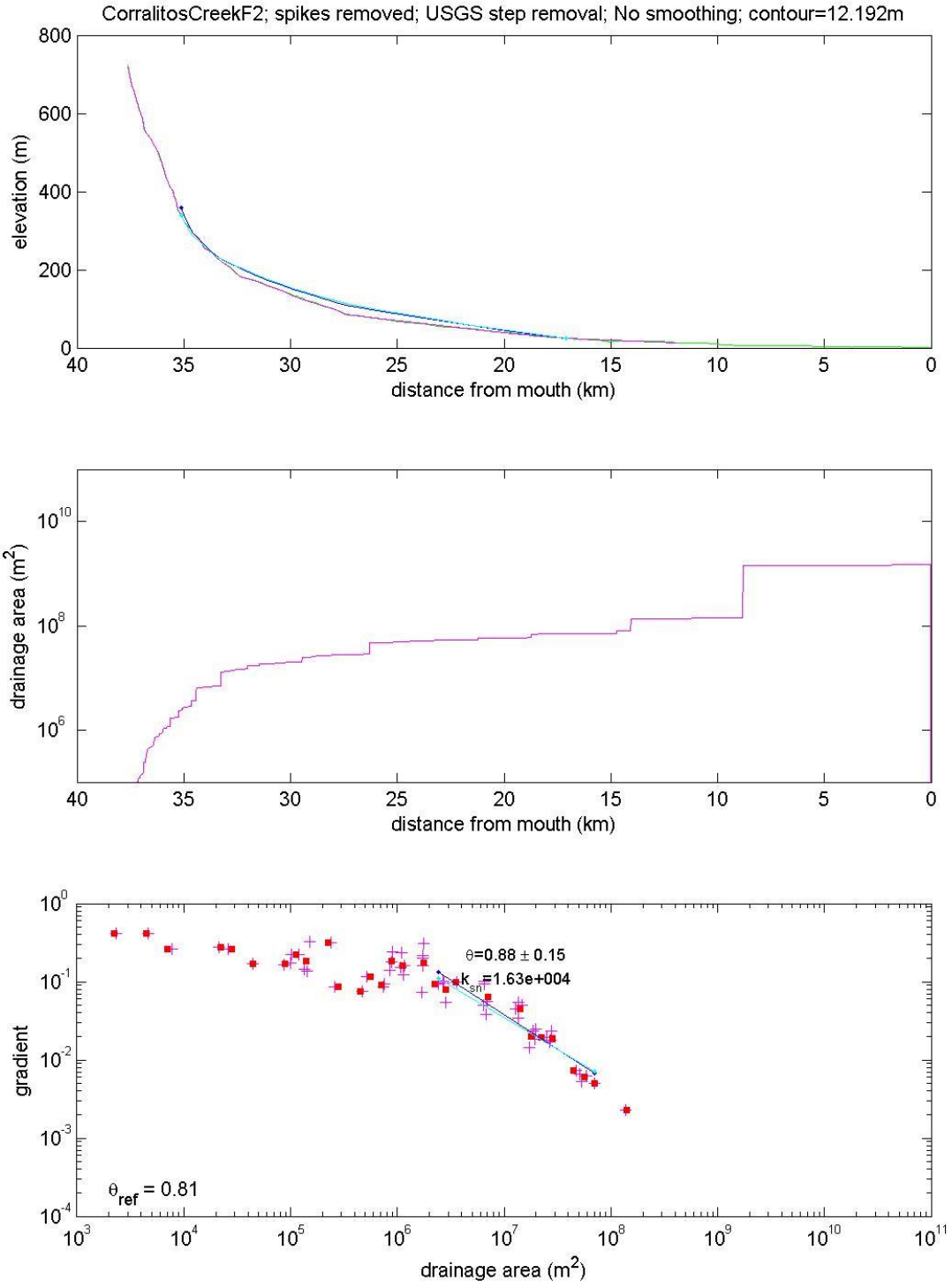
CorralitosCreekF2; spikes removed; USGS step removal; No smoothing; contour=12.192m
elevation (m)
distance from mouth (km)
drainage area (m2)
distance from mouth (km)
gradient
θ=0.88 ± 0.15
ksn=1.63e+004
θref = 0.81
drainage area (m2)

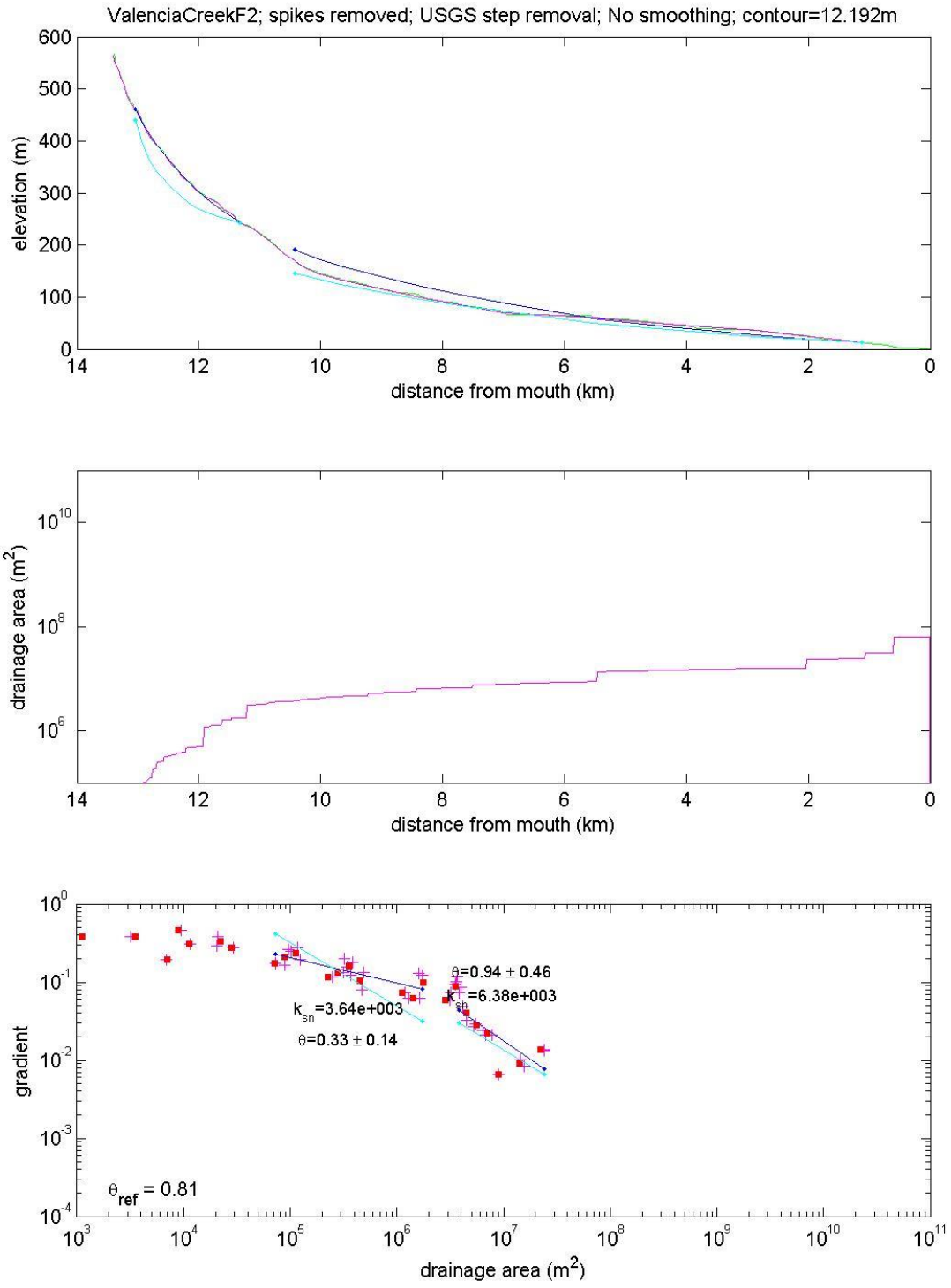
ValenciaCreekF2; spikes removed; USGS step removal; No smoothing; contour=12.192m
elevation (m)
distance from mouth (km)
drainage area (m2)
distance from mouth (km)
gradient
drainage area (m2)
θ=0.94 ± 0.46
ksn=6.38e+003
ksn=3.64e+003
θ=0.33 ± 0.14
θref = 0.81

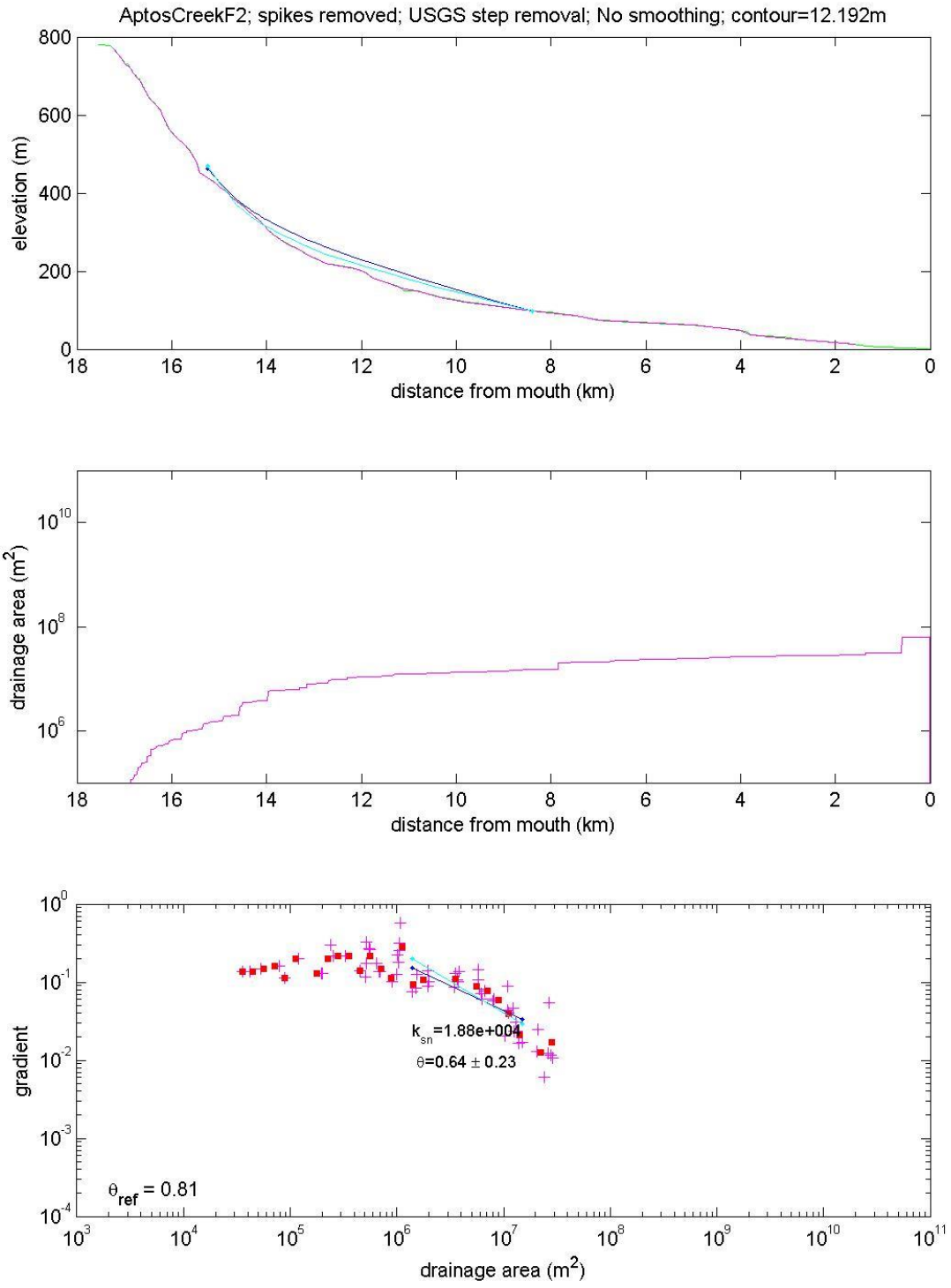
AptosCreekF2; spikes removed; USGS step removal; No smoothing; contour=12.192m
elevation (m)
distance from mouth (km)
drainage area (m2)
distance from mouth (km)
gradient
ksn=1.88e+004
θ=0.64 ± 0.23
θref = 0.81
drainage area (m2)

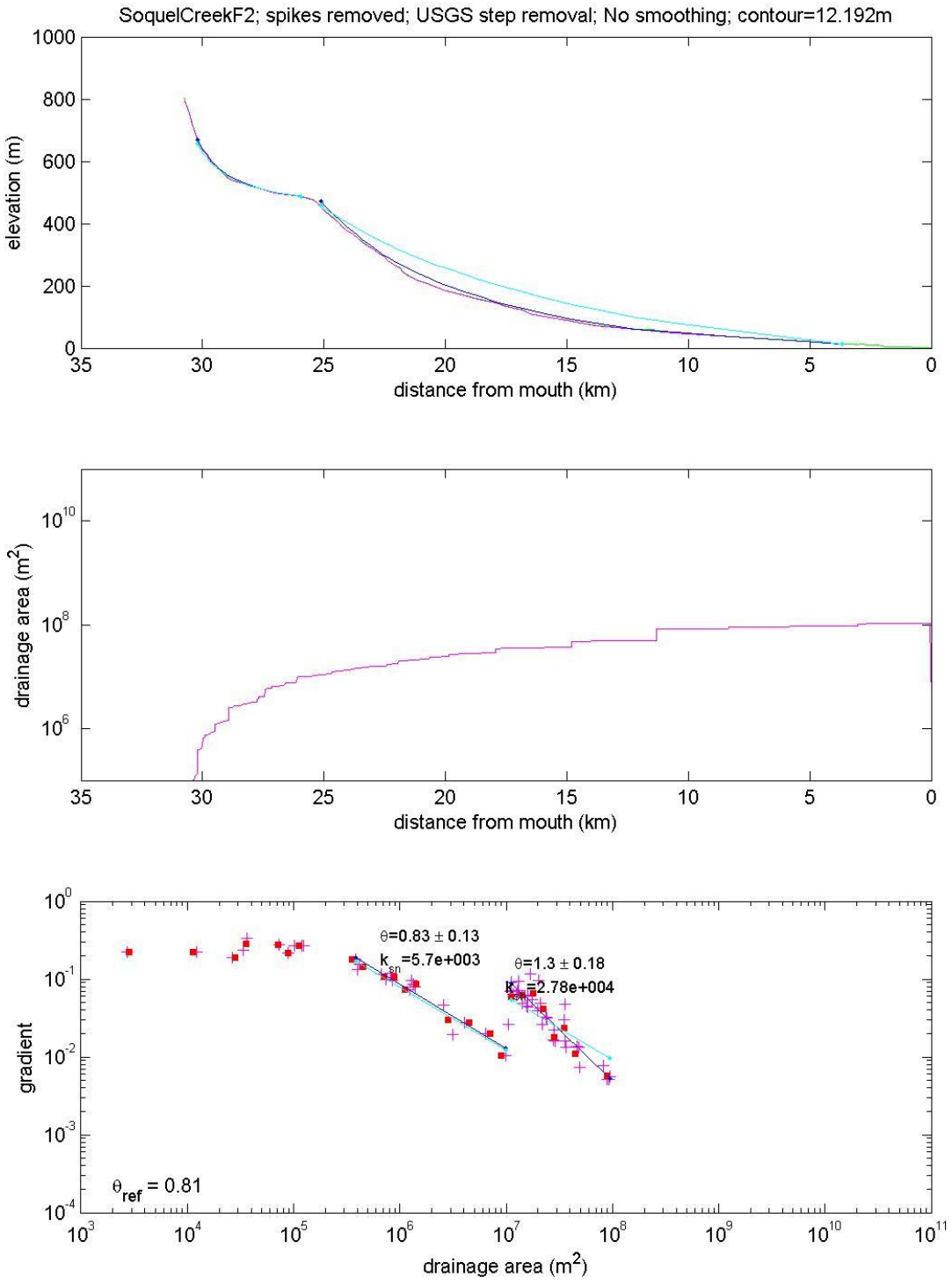
SoquelCreekF2; spikes removed; USGS step removal; No smoothing; contour=12.192m
elevation (m)
distance from mouth (km)
drainage area (m2)
distance from mouth (km)
gradient
θ=0.83 ± 0.13
ksn=5.7e+003
θ=1.3 ± 0.18
ksn=2.78e+004
θref = 0.81
drainage area (m2)

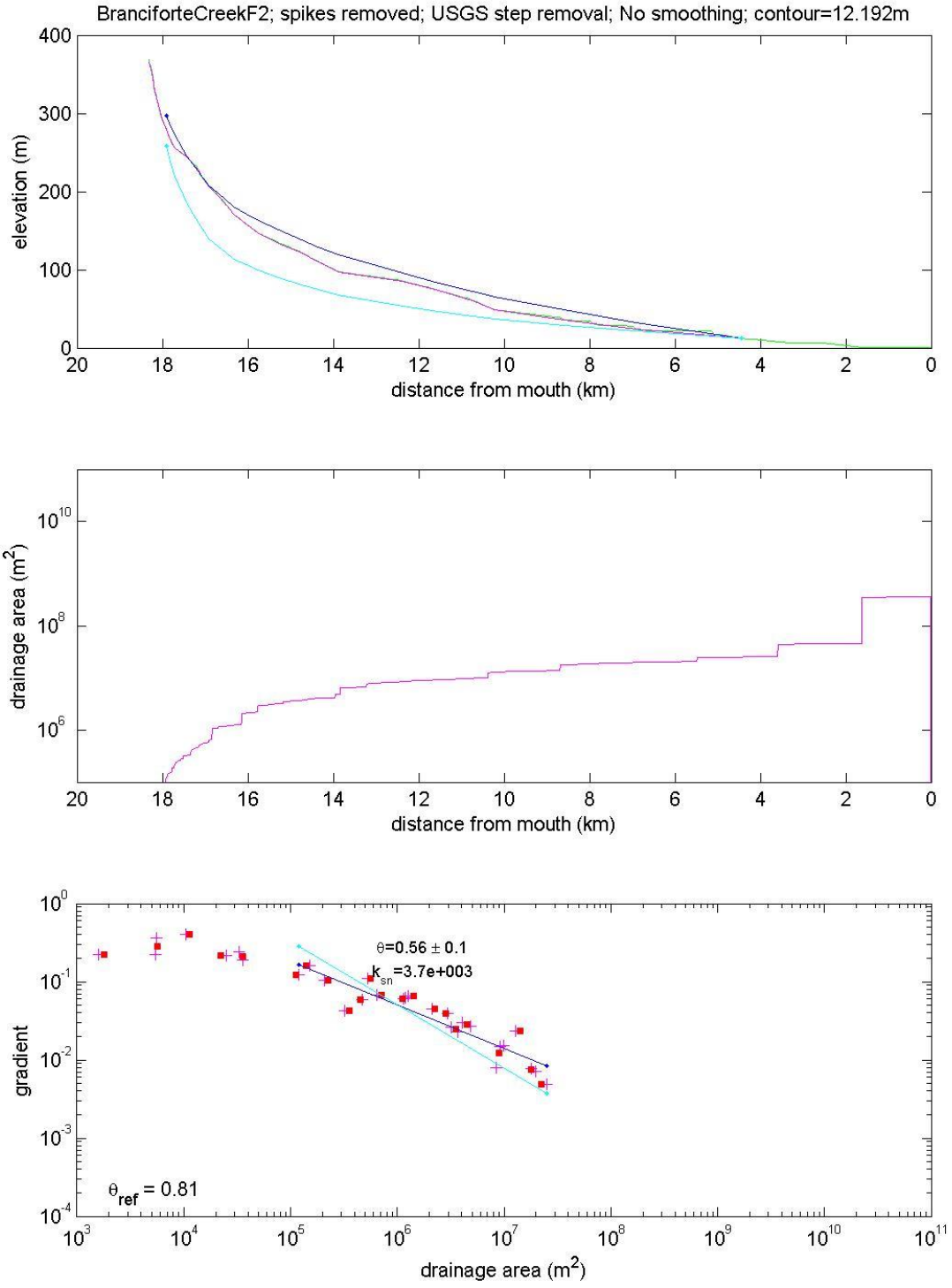
BranciforteCreekF2; spikes removed; USGS step removal; No smoothing; contour=12.192m
elevation (m)
distance from mouth (km)
drainage area (m2)
distance from mouth (km)
gradient
θ=0.56 ± 0.1
ksn=3.7e+003
θref = 0.81
drainage area (m2)

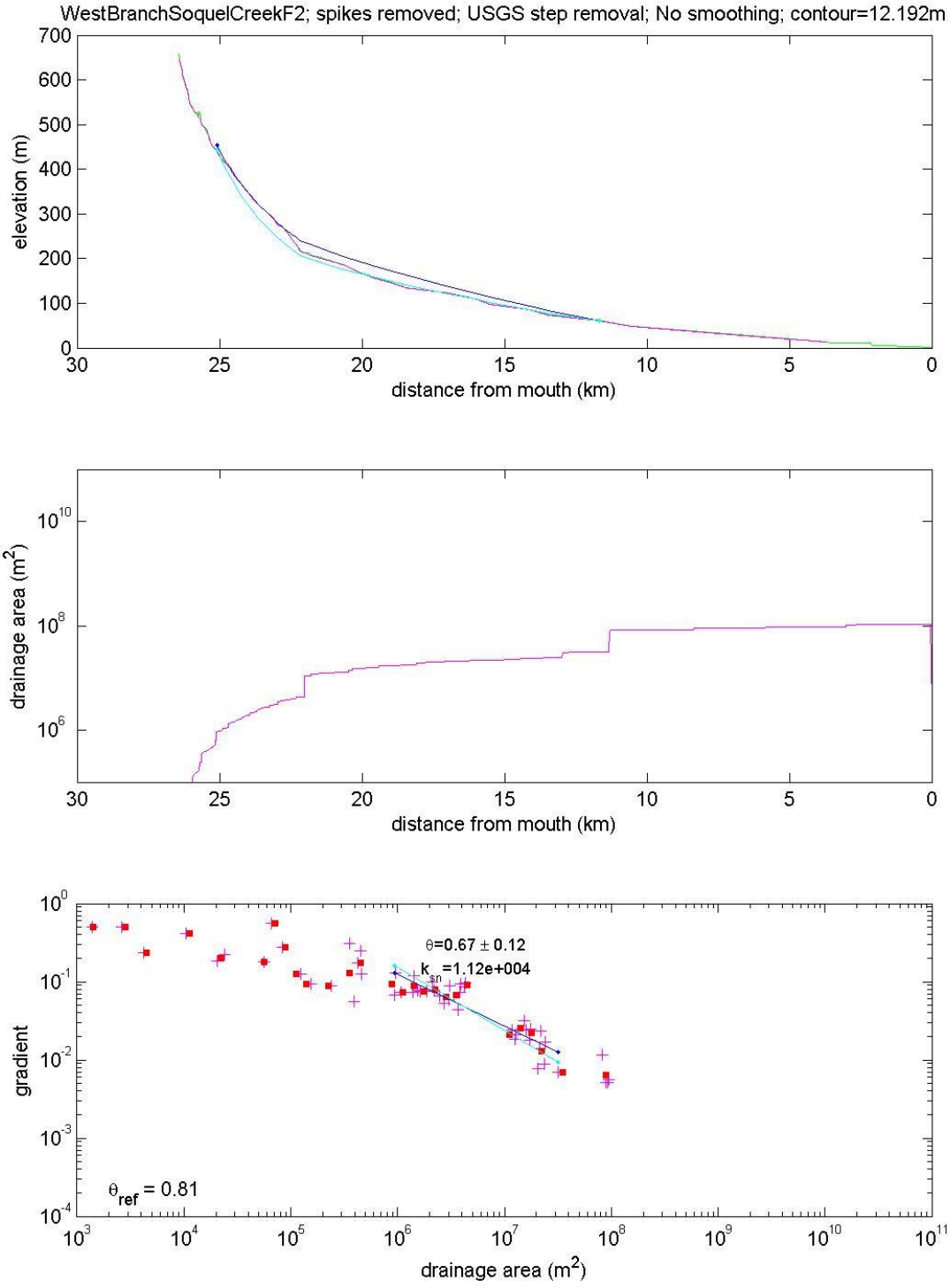
WestBranchSoquelCreekF2; spikes removed; USGS step removal; No smoothing; contour=12.192m
elevation (m)
distance from mouth (km)
drainage area (m2)
distance from mouth (km)
gradient
θ=0.67 ± 0.12
k_sn =1.12e+004
θref = 0.81
drainage area (m2)

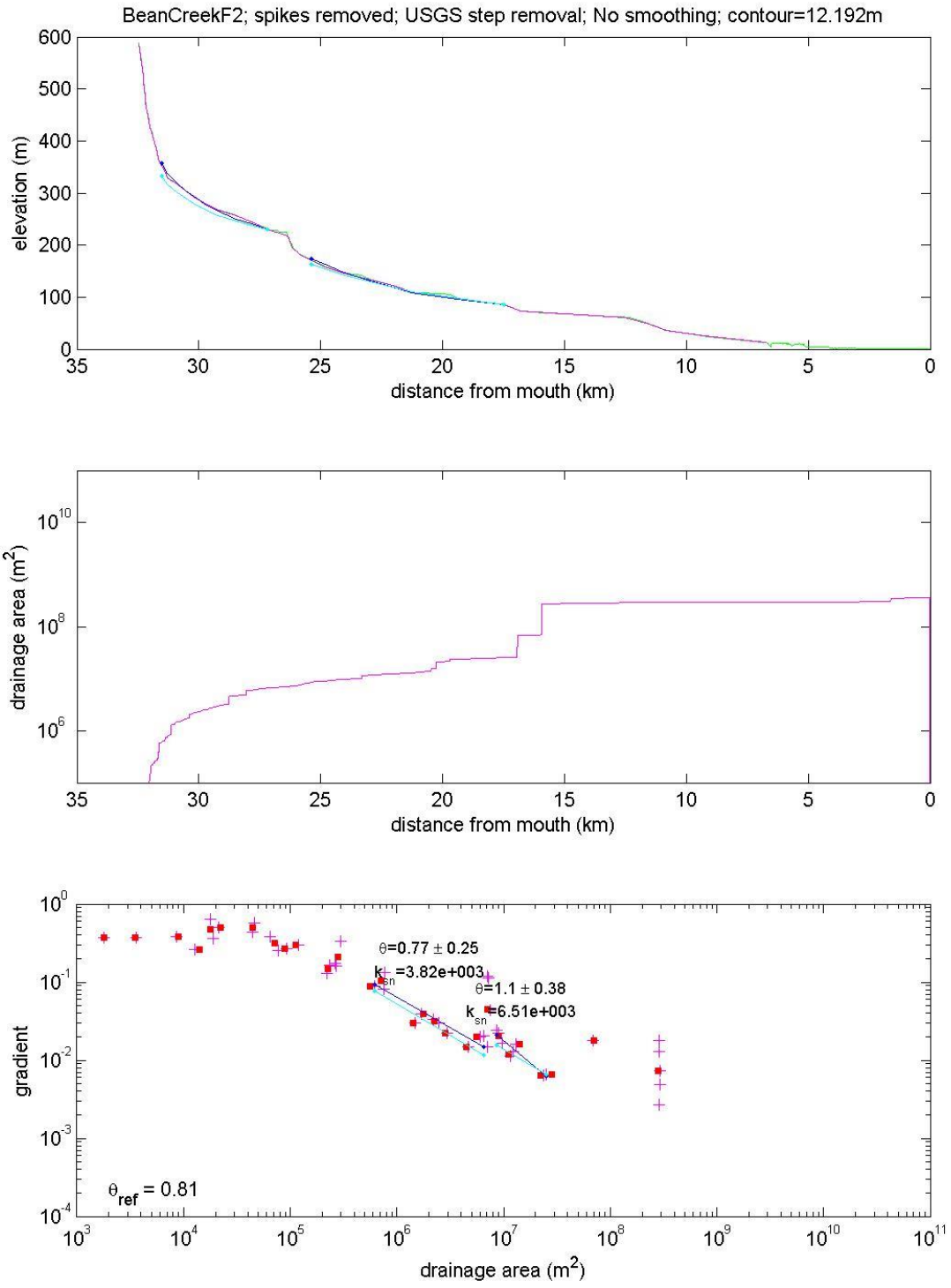
BeanCreekF2; spikes removed; USGS step removal; No smoothing; contour=12.192m
elevation (m)
distance from mouth (km)
drainage area (m2)
distance from mouth (km)
gradient
θ=0.77 ± 0.25
ksn=3.82e+003
θ=1.1 ± 0.38
ksn=6.51e+003
θref = 0.81
drainage area (m2)

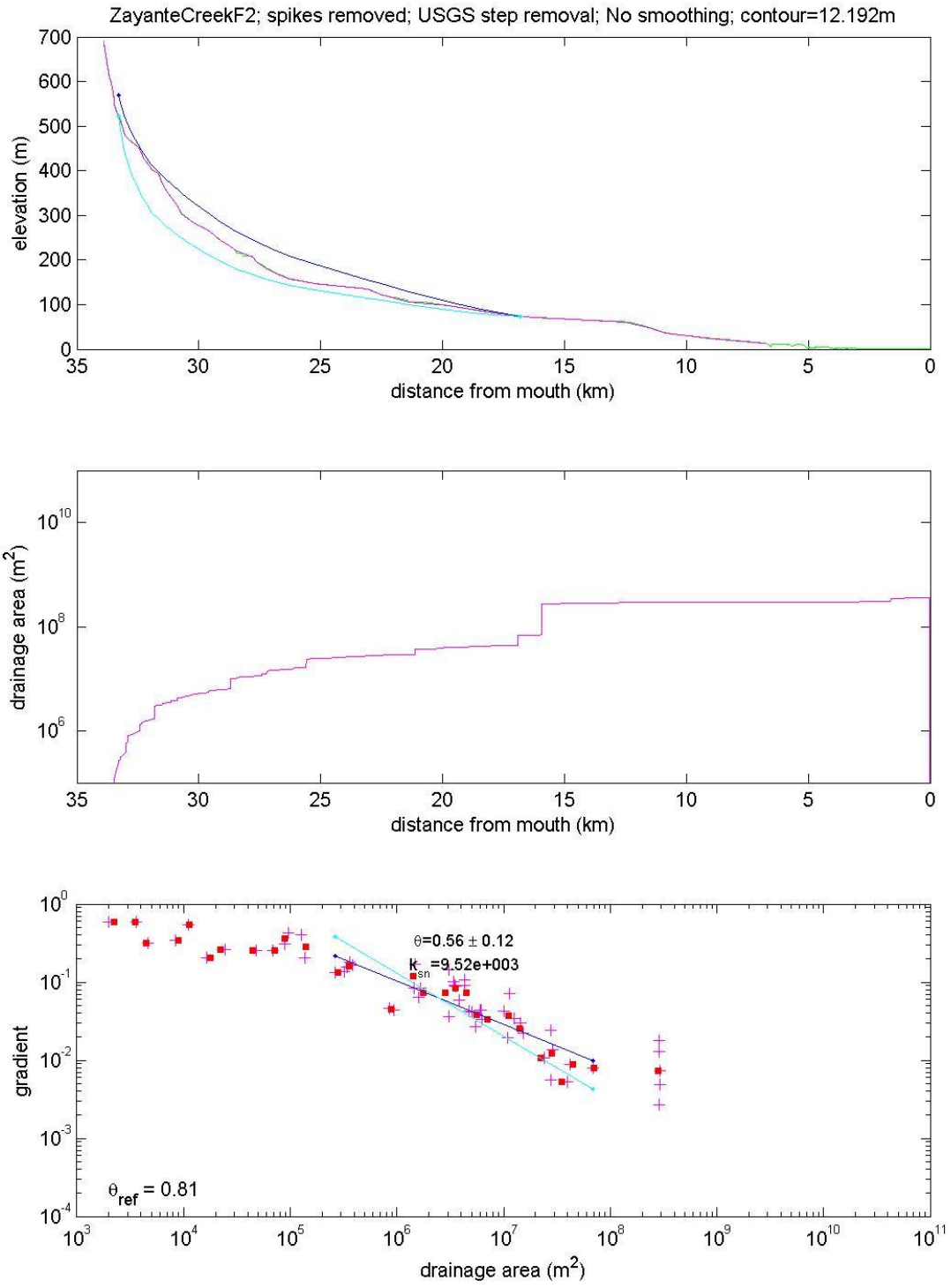
ZayanteCreekF2; spikes removed; USGS step removal; No smoothing; contour=12.192m
elevation (m)
distance from mouth (km)
drainage area (m2)
distance from mouth (km)
gradient
θ=0.56 ± 0.12
ksn =9.52e+003
θref = 0.81
drainage area (m2)

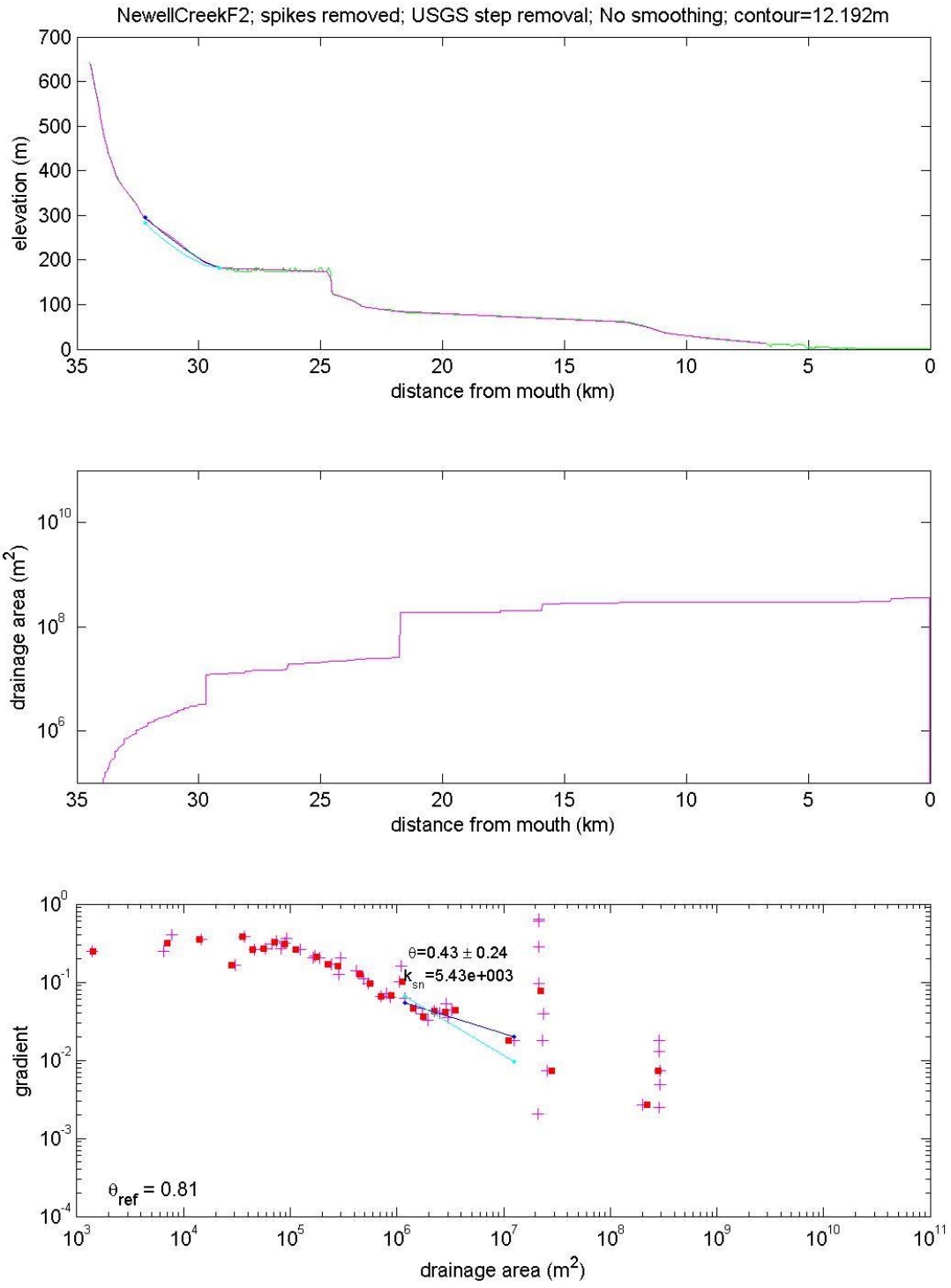
NewellCreekF2; spikes removed; USGS step removal; No smoothing; contour=12.192m
elevation (m)
distance from mouth (km)
drainage area (m2)
distance from mouth (km)
θ=0.43 ± 0.24
ksn=5.43e+003
θref = 0.81
gradient
drainage area (m2)

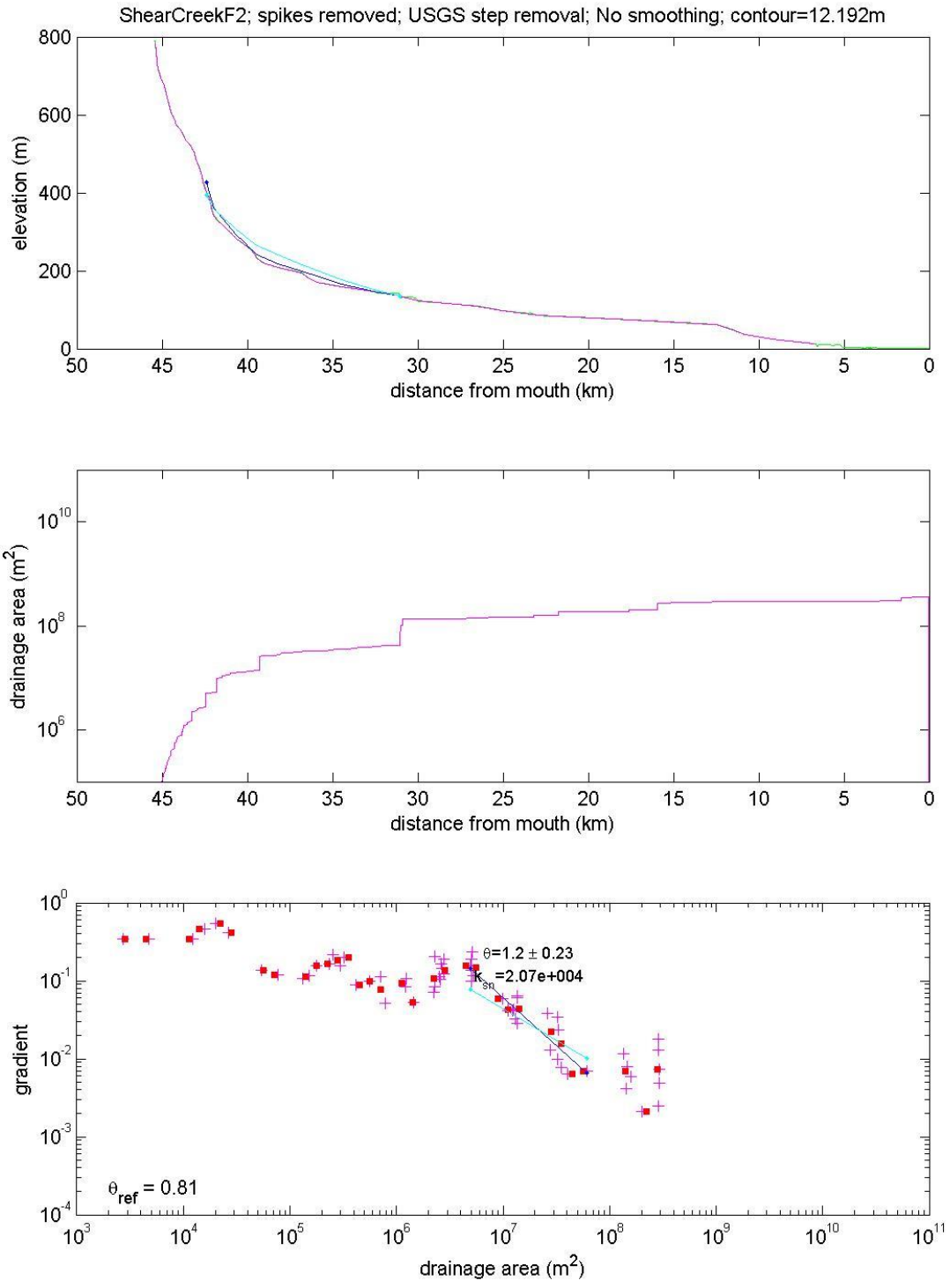
ShearCreekF2; spikes removed; USGS step removal; No smoothing; contour=12.192m
elevation (m)
distance from mouth (km)
drainage area (m2)
distance from mouth (km)
gradient
θ=1.2 ± 0.23
ksn=2.07e+004
θref = 0.81
drainage area (m2)

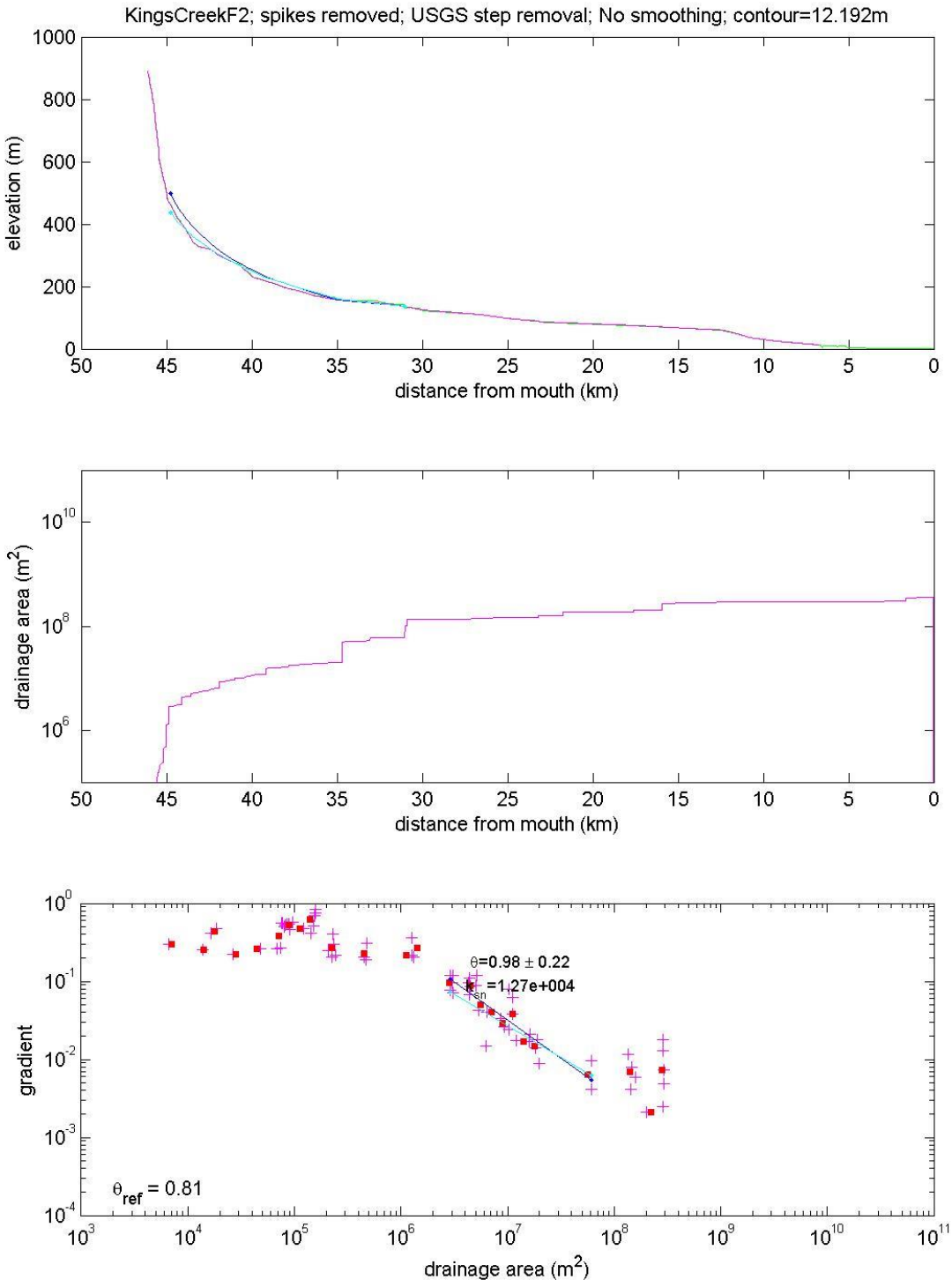
KingsCreekF2; spikes removed; USGS step removal; No smoothing; contour=12.192m
elevation (m)
distance from mouth (km)
drainage area (m2)
distance from mouth (km)
gradient
θ=0.98 ± 0.22
ksn=1.27e+004
θref = 0.81
drainage area (m2)

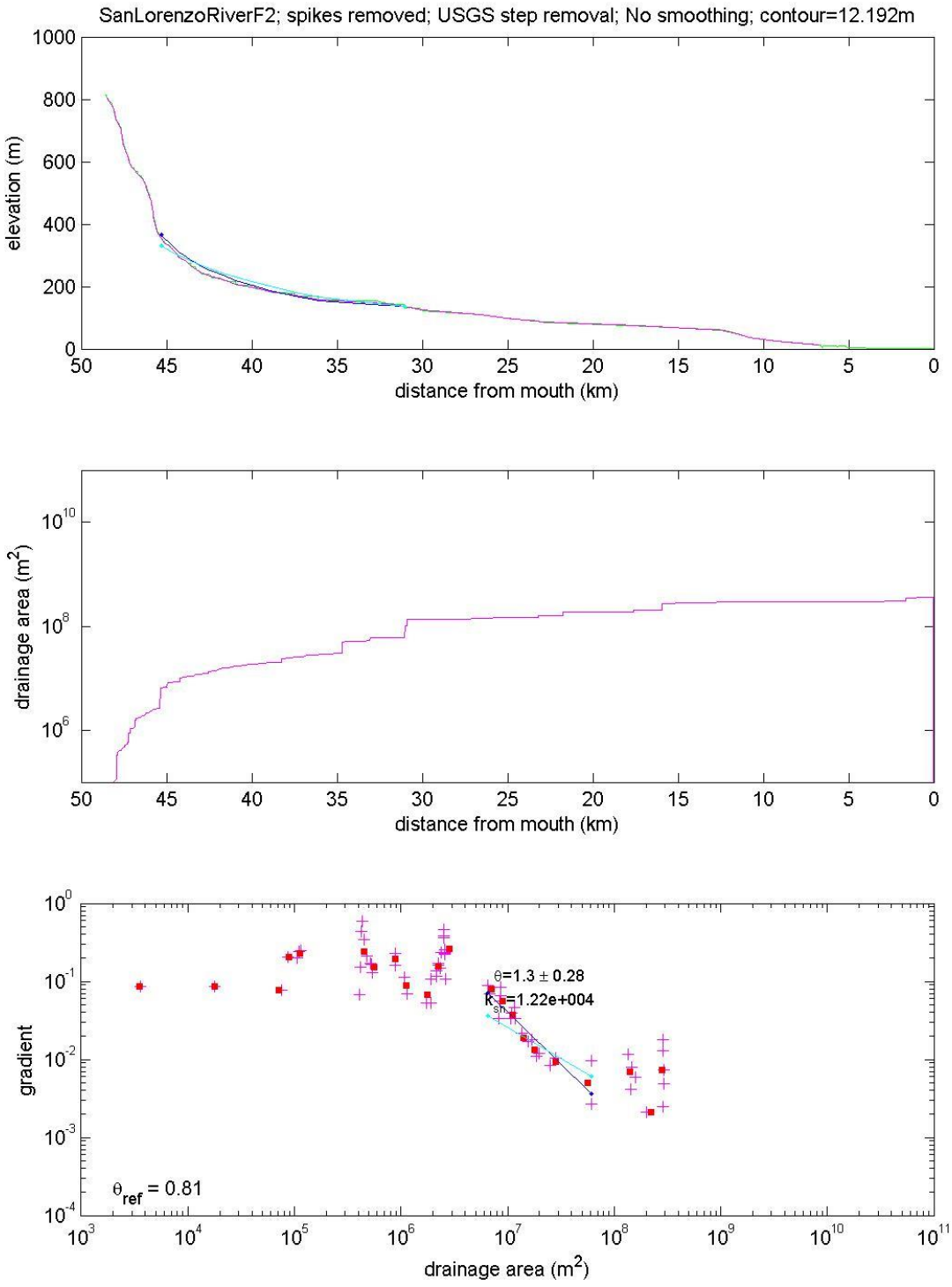
SanLorenzoRiverF2; spikes removed; USGS step removal; No smoothing; contour=12.192m
elevation (m)
distance from mouth (km)
drainage area (m2)
distance from mouth (km)
gradient
θ=1.3 ± 0.28
θref = 0.81
drainage area (m2)